Materials Chemistry and Physics 136 (2012) 394–414

Contents lists available at SciVerse ScienceDirect

Materials Chemistry and Physics

journal homepage: www.elsevier.com/locate/matchemphys

Corrosion and wear resistance of hypoeutectic Zn–Al alloys as a function of structural features

A.E. Ares [a,b,*], L.M. Gassa [a,c], C.E. Schvezov [a,b], M.R. Rosenberger [a,b]

[a] Career of Scientific Research (CIC) of the National Science Research Council of Argentina (CONICET), Argentina
[b] Faculty of Sciences, University of Misiones, 1552 Félix de Azara Street, 3300 Posadas-Misiones, Argentina
[c] The Research Institute of Theoretical and Applied Physical Chemistry (INIFTA), National University of La Plata-CONICET, Suc 4, C.C. 16, (1900) La Plata, Argentina

HIGHLIGHTS

- A combined study encompassing the grain and dendritic scale was here performed.
- The results include corrosion as well as wear parameters.
- Even at the highest Al wt%, the corrosion resistance depends on the structure.
- The wear resistance increases from the columnar to the equiaxed structure.
- A clear inverse relation is observed between the wear resistance and λ_2.

ARTICLE INFO

Article history:
Received 2 September 2011
Received in revised form
2 June 2012
Accepted 29 June 2012

Keywords:
Alloys
Solidification
Tribology and wear
Corrosion test
Microstructure
Corrosion
Mechanical properties

ABSTRACT

The aim of the present research was to investigate the role of the type of grain macrostructure (columnar, columnar-to-equiaxed transition–CET -, and equiaxed) and microstructure (secondary dendrite arm spacing - λ_2) in the wear and electrochemical behavior of hypereutectic Zn–Al alloys (Zn-1wt%Al, Zn-2wt%Al, Zn-3wt%Al and Zn-4wt%Al) directionally solidified in a vertical upward directional solidification device. We also aimed to, correlate the thermal parameters with the electrochemical and wear properties. The results obtained in this alloy system indicate that the corrosion resistance decreases as the concentration of aluminum increases, but that at the highest concentrations (near the eutectic concentration) this resistance depends on the structure. For the same wear conditions, the wear rate of the equiaxed region is lower than the columnar and transition regions. Independently of the type of structure, wear resistance increases as the aluminum concentration increases.

For each alloy concentration, the wear resistance increases from the columnar to the equiaxed structure. A clear inverse relation is observed between the wear resistance and λ_2, which may explain the increase in wear resistance in the equiaxed region. At low spacings, the wear rate converges to a single value.

1. Introduction

Most manufacturing processes involve melting and solidification of metals and alloys during the fabrication of various components. The thermal and solutal conditions that prevail during the manufacturing process and the thermodynamic and kinetic constraints of the material determine the final microstructure of the component. Solidification involves the extraction of heat from the liquid and the motion of the solid–liquid interface. The solidification rate is determined mainly by heat extraction through thermal diffusion and convection. However, the solidification microstructure is a complex function of the composition of the alloy, the solidification rate, the heat extraction flow, the temperature gradients, and several material characteristics such as phase equilibrium reactions, nucleation and growth kinetics of the phases and crystallographic constraints.

A typical cast structure consists of one or both types of grains: columnar or equiaxed. When both are present, the columnar is the first to solidify and then the equiaxed grains are usually formed in the central part of the cast. In such case, the transition is defined as columnar-to-equiaxed transition (CET). A low solidification rate favors the CET phenomenon as well as the addition of nucleant particles [1].

* Corresponding author. Faculty of Sciences, University of Misiones, 1552 Félix de Azara Street, 3300 Posadas-Misiones, Argentina. Tel.: +54 3752 422186x156; fax: +54 3752 425414.
E-mail addresses: aares@fceqyn.unam.edu.ar, a.e.ares@gmail.com (A.E. Ares).

0254-0584/$ – see front matter © 2012 Elsevier B.V. All rights reserved.
http://dx.doi.org/10.1016/j.matchemphys.2012.06.065

During many manufacturing processes, the CET is normally avoided because the casting must usually consist of only one type of grain; for instance, columnar in the case of turbine blades and equiaxed in the case of car engine parts.

The macrostructure of cast alloys is determined by process parameters such as the superheat, alloy system, composition, casting size, fluid flow, addition of grain refiner, and mechanical disturbance [2]. Although the directional solidification process is controlled mainly by temperature gradients and an important contribution of flow, the structure is mostly affected by the combined effect [1,2].

However, the CET structure is frequently not required and it is very important to understand the interaction of equiaxed grains between themselves and with the columnar front. In addition, it is important to understand the physical mechanisms which control the phenomenon and to link the parameters characterizing the CET during the directional solidification process with mechanical and corrosion properties of each type of structure (columnar, CET and equiaxed).

A number of experimental investigations have suggested that the CET occurs when the temperature gradient in the melt reaches a minimum critical value [1–13]. Gandin [14] proposed a CET criterion based on the position of the maximum velocity of the columnar/dendritic interface, suggesting a continuous increase in tip growth rates up to a maximum value about two-thirds the length of the ingot, where the transition is supposed to occur. We have previously investigated experimentally the directional solidification of Al–Zn and Zn–Al alloys under different conditions of superheat [15] and found that the results are related to the solidification thermal parameters and recalescence determined from the temperature versus time curves. The observations indicate that the CET is the result of a competition between coarse columnar dendrites and finer equiaxed dendrites. The experiments carried out by Nguyen-Thi et al. [16] on Al-3.5wt%Ni alloy provided direct access to dynamical phenomena during columnar growth, and for the first time to the CET microstructure. In those experiments, the dendritic morphologies were analyzed as a function of the solidification parameters. Siqueira et al. [5,17] and Spinelli et al. [18] proposed a CET criterion based on critical cooling rate of about 0.014 K s^{-1} and 0.030 K s^{-1}, respectively, with the columnar growth prevailing throughout the casting for cooling rates higher than these critical values. Badillo and Beckermann [19] developed a study to perform direct numerical simulations of the CET in two spatial dimensions, of the CET in directional solidification of an Al–3wt%Cu alloy using the phase-field model.

The results illustrate the full complexities of the solute concentration fields and solidification morphologies. Canté et al. [20] conducted experiments to examine the CET during the upward vertical directional solidification of hypoeutectic Al–Ni and Al–Sn alloys under unsteady-state heat flow conditions and noted that the CET occurs essentially on a near horizontal plane in the castings when critical cooling rate in the melt is reached. For the investigated alloys the average critical values were found to be about 0.16 K s^{-1} for the Al–Ni alloys and 0.30 K s^{-1} for the Al–Sn alloys.

Other previous studies of the CET develop expressions, simulations and numerical procedures to describe a criterion for the CET [17,19,21–34].

It is well known that convection influences the CET and primary cellular/dendritic spacings. Natural convection during solidification is principally caused by density gradients in the liquid. The temperature gradient in the liquid may lead to thermal convection and the rejected solute in the interdendritic liquid may cause solutal convection. Whether the thermal and solutal buoyancy forces may either counteract or increase each other depending on the relative densities of the alloy constituents and the particular constituent rejected into the interdendritic liquid during solidification [35,36].

The uses of Zn can be divided into six major categories: (a) coatings, (b) casting alloys, (c) alloying element in brass and other alloys, (d) wrought zinc alloys, (e) zinc oxide, and (f) zinc chemicals. The binary zinc alloy systems of most interest for commercial applications are Zn–Al, which at 4wt.%Al form the basis of the zinc die-casting alloys. Cast zinc products are produced mainly by die-casting process, in which the liquid metal is forced under pressure into a cooled die and solidifies almost instantaneously to produce a fine-grained product. One unique application of zinc takes particular advantage of its ability to transfer its corrosion resistance properties by electrical contact. This application is called a sacrificial anode. The anodes, made of almost pure zinc, are bolted to aluminum marine engines. During operation in water, especially salt water, the oxidation forms a weak electrical current, which may corrode the hull and engine parts. Since zinc is easily oxidized in the presence of this electrical current, it "sacrifices" itself by corroding quickly, consuming the entire electrical imbalance in the ship. As a result, the remaining aluminum hull and engine are not corroded as a result. As it is consumed, the anode must be replaced to assure continued protection. In an application similar to the sacrificial anode, zinc is used as a component in battery production [37].

One particular area of research has been dedicated to the relationship between the properties and the cast structure. Sahoo et al. [38], Prasad et al. [39] and Sriram et al. [40] investigated the effects of trace elements on the casting characteristics and mechanical properties of cast Zn–Al alloys, and found that ultimate tensile strength, yield strength and percent elongation of the alloys are slightly lower in Sr-treated melts, but higher when Be is added. They also found that hardness values increase when Be is added, that impact strength is drastically reduced when Sr and B are added, and that the elongation and impact strength are improved when Sr and B are added.

Osorio et al. [41] studied the role of macrostructural morphology and grain size in the corrosion resistance of Zn and Al castings and concluded that a better corrosion resistance tendency is achieved with coarse macrostructures rather than with fine grains for both Zn and Al. When studying the effect of the dendritic microstructure of the corrosion resistance of Zn–Al alloys Osorio et al. [42] found that the tendency of improvement on the corrosion resistance depends both on the cooling rate imposed during solidification, which affects dendrite arm size and the solute redistribution, and on the electrochemical behavior of solute and solvent. In addition, by studying the application of electrochemical impedance spectroscopy to investigate the effect of as-cast structures on the corrosion resistance of hypereutectic Zn–Al alloys, these authors showed that the corrosion resistance of hypereutectic Zn–Al alloys tends to improve as the dendritic arm spacing increases and that the impedance parameters of both zones (columnar and equiaxed) are similar. In their experiments, the CET occurred in a sharp plane which did not yield a mixed structure and therefore did not characterize the properties of the mixed structure formed with columnar and equiaxed grains [43].

Abou El-khair et al. [44] studied the effects of different Al contents on the microstructure, hardness, tensile properties and wear behavior of Zn-based alloys and found that the hardness of Zn–Al alloys increases as Al content is increased from 8 to 27 wt.%, and that there is a significant improvement in ultimate strength at room and high temperatures.

Auras and Schvezov [45] studied the influence of alloying elements and SiC particles in the solidification process, alloy morphology, wear mechanism and debris formation in ZA27-based alloys containing silicon and copper and found the following: that

the Si precipitates appear in a plate-like shape in the dendrites or grain, that the cooper appears in the solution at concentrations lower than 1 pct and as a precipitate in the interdendritic at higher concentrations, and that the SiC particles appear in the interdendritic regions.

Manna et al. [46–50] studied the formation of a precipitate phase β and a solute depleted matrix phase α behind a migrating boundary advancing into a supersaturated matrix phase α_0 which is called discontinuous precipitation (DP) [51] and found that the precipitation is characterized by discontinuous discontinuous changes in orientation and composition between the matrix phases (α_0/α) across the migrating boundary, called the reaction front (RF), which provides a short-circuit path of solute transport [51–53]. They also found that the Zn-2at.%Ag alloy undergoes a discontinuous mode of precipitation in the temperature range of 353–433 K.

The rod-like precipitate phase in the DP colony maintains a distance of separation statistically constant under isothermal conditions of precipitation. This approach has already been applied in several binary systems like Zn–Al [54] and other systems [55–58].

In previous works, we studied the influence of thermal parameters on the structure and CET transition [13,15,32,59] and measured the mechanical and corrosion properties of the alloys with different structures [60,61]. Our main results indicated that the CET occurs in a zone rather than in a sharp plane, where both columnar and equiaxed grains coexist with the melt, and that the length of the columnar zone increases with the cooling rate and decreases with alloy composition, which could be associated with the kinetics of solidification. Also, the CET was observed to occur when the temperature gradient in the melt decreased to values close to zero with some gradients being slightly negative. In addition, we observed that the velocity of the liquidus front was faster than that of the solidus front, which increased the size of the mushy zone.

We have also previously found that the recalescence or thermal arrest and negative gradients in the transition zone are observed. After the transition, the speed of the liquidus front is much faster than that of the solidus front. The size of the equiaxed crystal is always smaller in the transition zone and then normally increases. The average secondary spacing increases from columnar to equiaxed zones in the samples. There is a linear and inverse correlation between the yield strength (YS), maximum tensile strength (TS) and Vickers microhardness (VH) and secondary dendrite arm spacing (λ_2), independently of the type of grains (columnar or equiaxed). YS, TS and VH depend differently on the grain size depending on the region considered: columnar or equiaxed.

Rosenberger et al. determined the wear resistance of Zn–1wt.% Al and Zn-2wt.% alloys using a pin-on-ring wear tests, as a function of type of structure of the as-cast alloys. The three regions were observed; columnar, equiaxed and CET. The results also showed that the equiaxed structure is the most resistant. In addition, the relation between wear rate and grain size depends on the type of structure and that it is more pronounced for the equiaxed structure. The effect was almost negligible for the columnar grain structure [62].

In previous works, we correlated the effect of several parameters, like thermal and metallurgical ones, with electrochemical parameters on the CET macrostructure in Zn-4wt.%Al, Zn-16wt.%Al and Zn-27wt.%Al alloys [63]. We were able to observed the susceptibility to corrosion of the alloys with columnar structure by analyzing the values of charge-transfer resistance (R_{ct}) obtained using the Electrochemical Impedance Spectroscopy (EIS) technique. In Zn-4wt%Al and Zn-27wt.%Al, the corrosion susceptibility depended on the structure of the alloy. The alloy with 16wt.%Al was the least resistant to corrosion and its susceptibility to corrosion was independent of the structure, whereas the alloy with 27wt.%Al and CET structure was the most resistant of all. By correlating the EIS parameters with thermal parameters like R_{ct} with the critical temperature gradient, G_c, we found that R_{ct} increases when G_c becomes more negative. In the case of the correlation between R_{ct} and structural parameters, i.e. grain size and secondary dendrite spacing, R_{ct} also increased when both parameters increased. This was not observed in Zn-16wt.%Al alloys.

Another recent research shows that what actually affects the response to corrosion is the way in which aluminum is distributed in the alloy, i.e., which phases are present in the solidified microstructure and how they are distributed, and not the amount of aluminum present in the alloy [64].

The above results show the strong relation between the solidification process parameters, the resulting structure and the mechanical and corrosion properties of the directionally solidified alloys.

The aims of the present research were to investigate the role of the type of grain macrostructure (columnar, CET and equiaxed) and microstructure (secondary dendrite arm spacing) in the wear and electrochemical behavior of hypereutectic Zn–Al alloys (Zn-1wt.% Al, Zn-2wt.%Al, Zn-3wt.%Al and Zn-4wt.%Al) directionally solidified in a vertical upward directional solidification device and to correlate the thermal parameters with the electrochemical and wear properties.

Table 1
Chemical composition of the Zn and Al used to prepare the alloys.

Element	Weight percent, wt%
Chemical composition of Zn	
Zn	99.98 ± 0.2
Fe	0.010 ± 0.01
Si	0.006 ± 0.0001
Pb	0.004 ± 0.001
Others	< 0.001 ± 0.0001
Chemical composition of Al	
Al	99.94 ± 0.2
Fe	0.028 ± 0.0001
Si	0.033 ± 0.001
Pb	0.001 ± 0.0001
Others	< 0.001 ± 0.0001

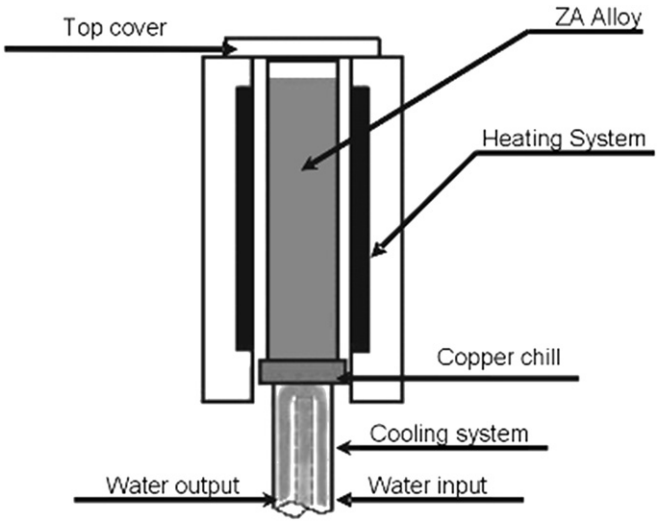

Fig. 1. Schematic illustration of the water-cooled vertical upward solidification setup.

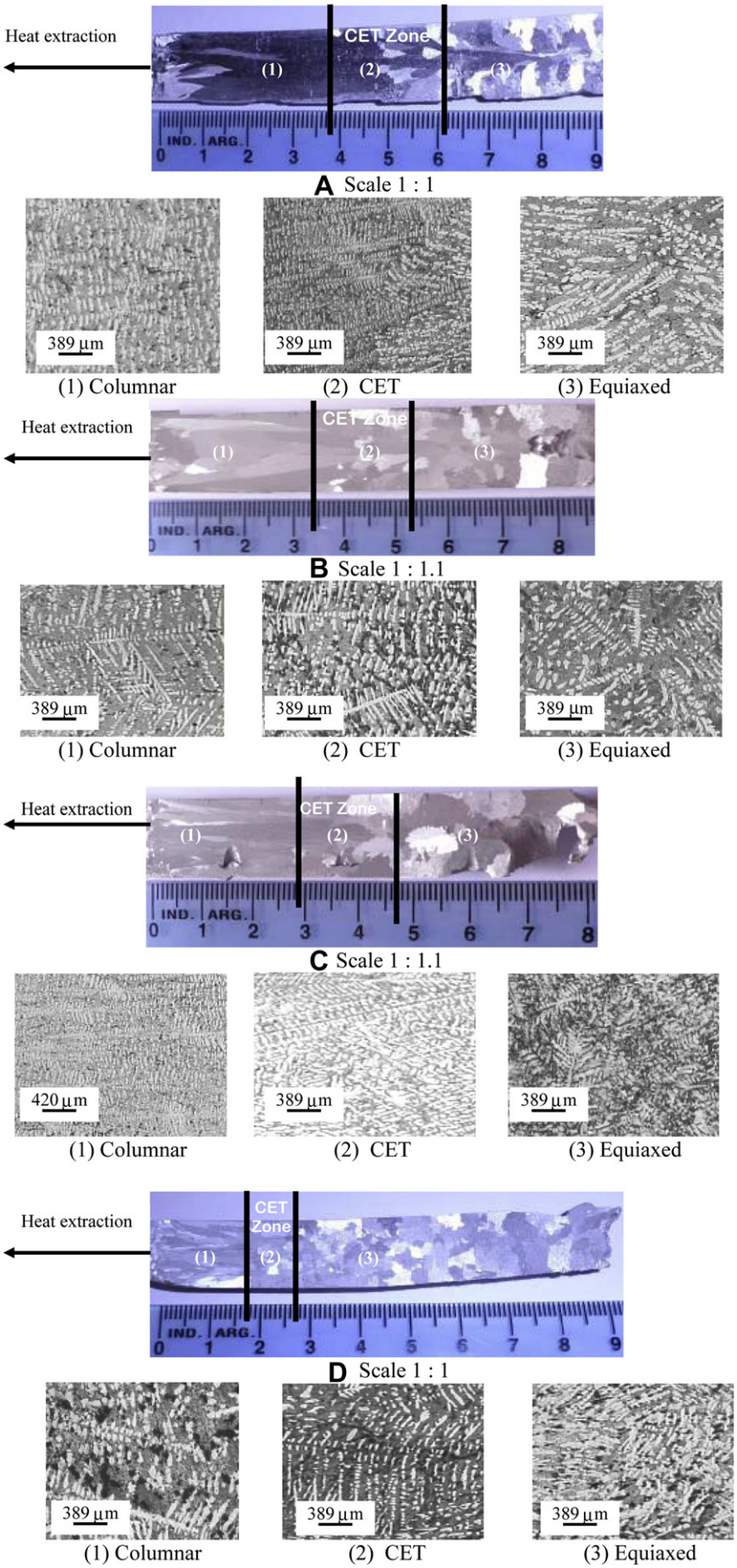

Fig. 2. Macrostructures: (A) Zn-1wt.%Al, (B) Zn-2wt.%Al, (C) Zn-3wt.%Al and (D) Zn-4wt.%Al, and microstructures of different alloy samples: (1) Columnar, (2) CET and (3) Equiaxed.

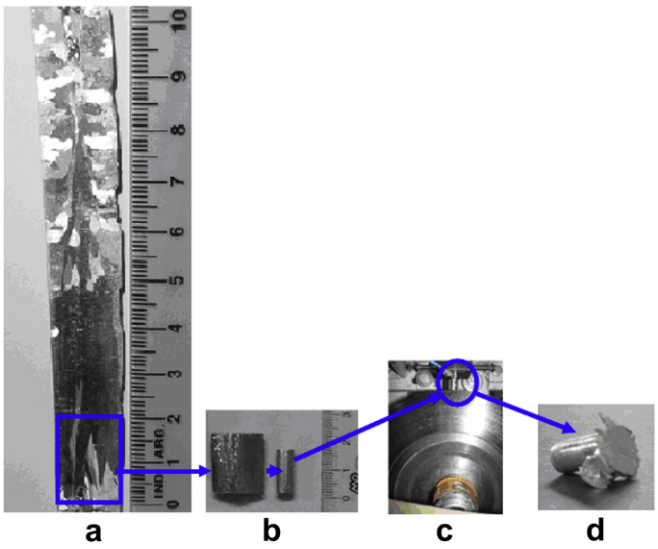

Fig. 3. (a) Directionally solidified sample of a Zn-1wt.%Al alloy showing the CET. (b) Pin preparation from columnar zone for wear test. (c) Pin position during the test. (d) Aspect of the pin after the wear test.

2. Experimental

2.1. Alloy preparation and directional solidification process

Experiments were performed with Zn–Al alloys prepared with four different solute contents; 1wt.%Al, 2wt.%Al, 3wt.%Al and 4wt.% Al. The chemical compositions of the commercially pure metals used to prepare the alloys are presented in Table 1. The molds were made from a 23 mm i.d. and 25 mm e.d. PYREX (Corning Glass Works, Corning, NY, USA) tube, with a flat bottom, a cylindrical uniform section and a height of 200 mm. The sample was a cylinder 22 mm in diameter and 100 mm in height.

The alloys were melted in a resistance-type furnace. The experimental setup consisted of a heat unit, a sample moving system, a heat extraction system, a temperature control and data acquisition systems (see schematic representation of Fig. 1). In order to understand the evolution of the thermal parameters during the solidification process, it was necessary to install thermocouples. One K-type thermocouple was used to control the temperature of the resistance furnace during the experiment and five K-type thermocouples were positioned at 20 mm intervals in the centerline of the cylinder mold from the bottom surface of the mold and were connected to a data acquisition system to record the temperature history of cooling.

The experimental procedure was as reported previously [15]. First, the liquid metal in the mold in the furnace was allowed to reach the selected temperature above the melting point of the alloy. Then, the furnace power was turned off and the melt was allowed to solidify from the bottom. Heat was extracted through a cooling system, which consisted of a copper disk attached to a copper coil, both cooled by running water. The solidification velocity was adjusted by changing the temperature and water flow and also by adding plates of materials between the copper plate and the crucible which changed the effective value of the thermal conductivity. The crucible was also isolated on the top to reduce heat losses from the top of the furnace to a minimum. With this experimental setup, unidirectional heat flow was achieved and the convection associated with the pouring of the liquid into the mold was eliminated.

Due to the formation of high pore density at the top of the cast sample and the formation of a shrinkage pipe, which increase with the aluminum concentration as reported by Barnhurst [65,66], the diluted concentrations of Zn–Al alloys selected for this study were: Zn-1wt.%Al, Zn-2wt.%Al, Zn-3wt.%Al and Zn-4wt.%Al. Also, for the same reason, only the first 100 mm height of the cast was considered for the sampling. After solidification, the cylinder samples were cut in the axial direction. One half was used to reveal the macrostructure and analyze the microstructure, whereas the other half was cut and machined in coupons 20 mm in length for the wear and corrosion tests.

2.2. Metallography

In order to reveal the macrostructure, the Zn–Al alloys were polished and etched using concentrated hydrochloric acid for approximately 30 s at room temperature, followed by rinsing and

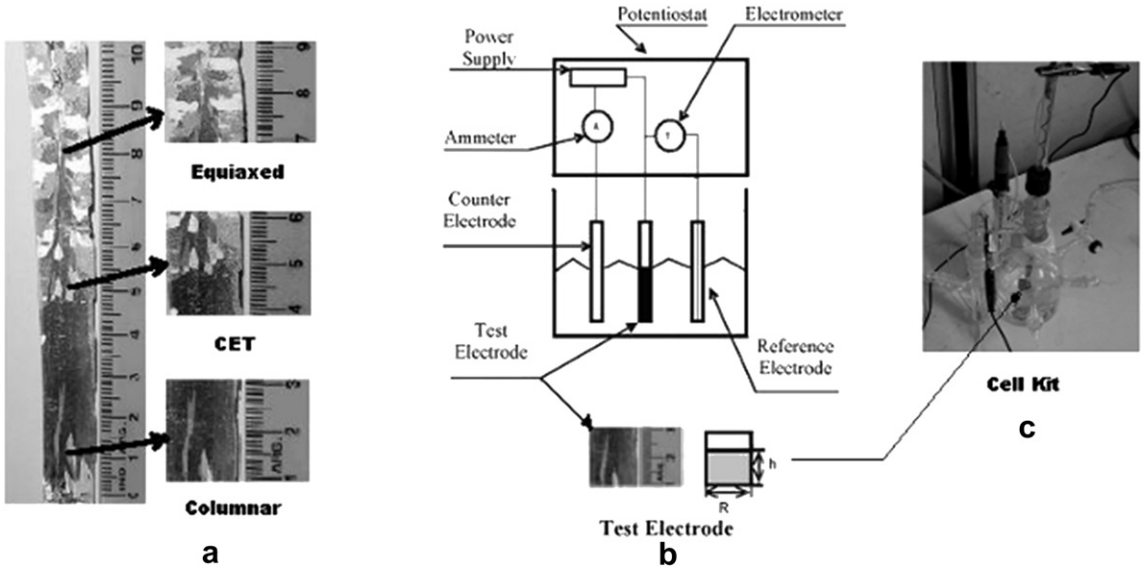

Fig. 4. (a) Test electrodes with different type of structures (columnar, equiaxed and CET). (b) Scheme of the position of the test electrode during the electrochemical tests and (c) Cell kit.

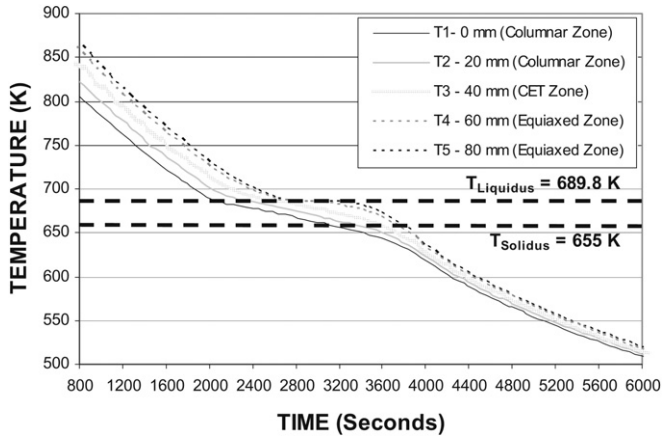

Fig. 5. Temperature versus time curves during directional solidification at different positions with respect to the chill.

wiping off the resulting black deposit. The selected surfaces were etched with a mix containing chromic acid (50 g Cr_2O_3; 4 g Na_2SO_4 in 100 ml of water) for 15 s at room temperature to reveal the microstructures [67]. As examples, the representative macro- and microstructures obtained in the different Zn–Al alloys are shown in Fig. 2. The numbers (1), (2) and (3) in each micrograph correspond to columnar, CET and equiaxed zones respectively.

The grain size (G_s) and secondary dendritic arm spacing (λ_2) were measured at each location using an Arcano® metallographic microscope and the Soft Imaging Solutions (former SIS) for digital image analysis and digital image management. The software offers the functions necessary for acquiring, further processing, interactive/automatic analysis, archiving and documentation of the digital images and related investigation results. The secondary dendrite arm spacings were measured by counting the number of branches along a line of known length [68]. The mean value of λ_2 was calculated from 15 measurements in each zone of the samples (columnar, equiaxed and CET).

To measure the equiaxed grain size from the CET zone to the top, each sample was divided into equal intervals. In each interval of approximately 10 mm, the average diameter of equiaxed grains was calculated according to the ASTM 112-96 standard norm [69]. The columnar region was divided into similar size intervals and the width and length of the columnar grains were measured directly from the samples.

2.3. Microhardness

Vickers microhardness was measured at room temperature using loads of 500 g_f. The measurements were performed under standard ASTM E 384-89 [69], using a pressing time of 15 s. The microhardness of each sample was determined along the longitudinal axis and every 20 mm by taken an average of 10 readings in each section of the sample.

2.4. Wear tests

The wear tests were performed in a pin-on-ring machine, consisting of a gray cast iron disc of 280 HV in hardness and 170 mm in diameter, which rotates giving a tangential velocity of 2.7 m s^{-1}. According to the pin-on-ring configuration, the disc axis is horizontally orientated and the pin is mounted vertically on top of the disc, on the curved edge. Fig. 3(a–d) shows the details of the wear tests.

Cylindrical pins 6.35 mm in diameter and 16 mm in length were used as samples. The pins were obtained from the casting ingots by

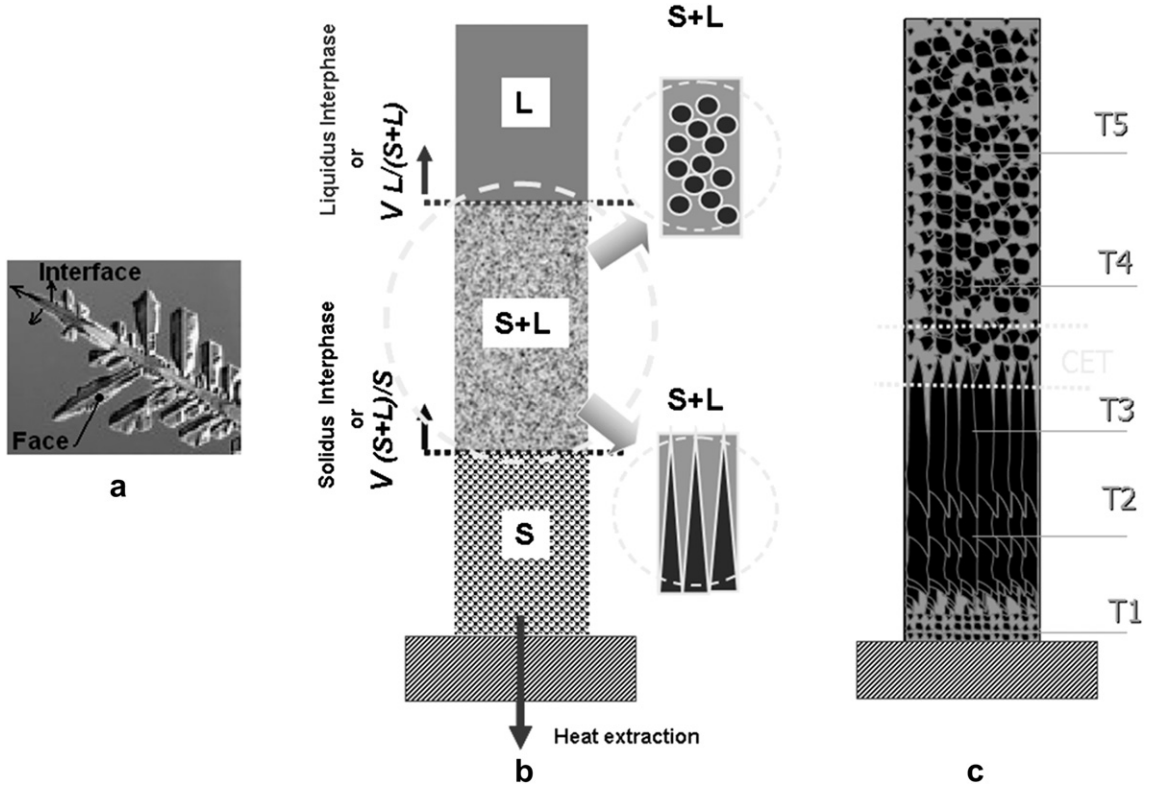

Fig. 6. Scheme (a) showing the face and interface in a dendrite tip, (b) showing the liquidus and solidus interphases in the sample and (c) showing a sample with the positions of thermocouple and the CET.

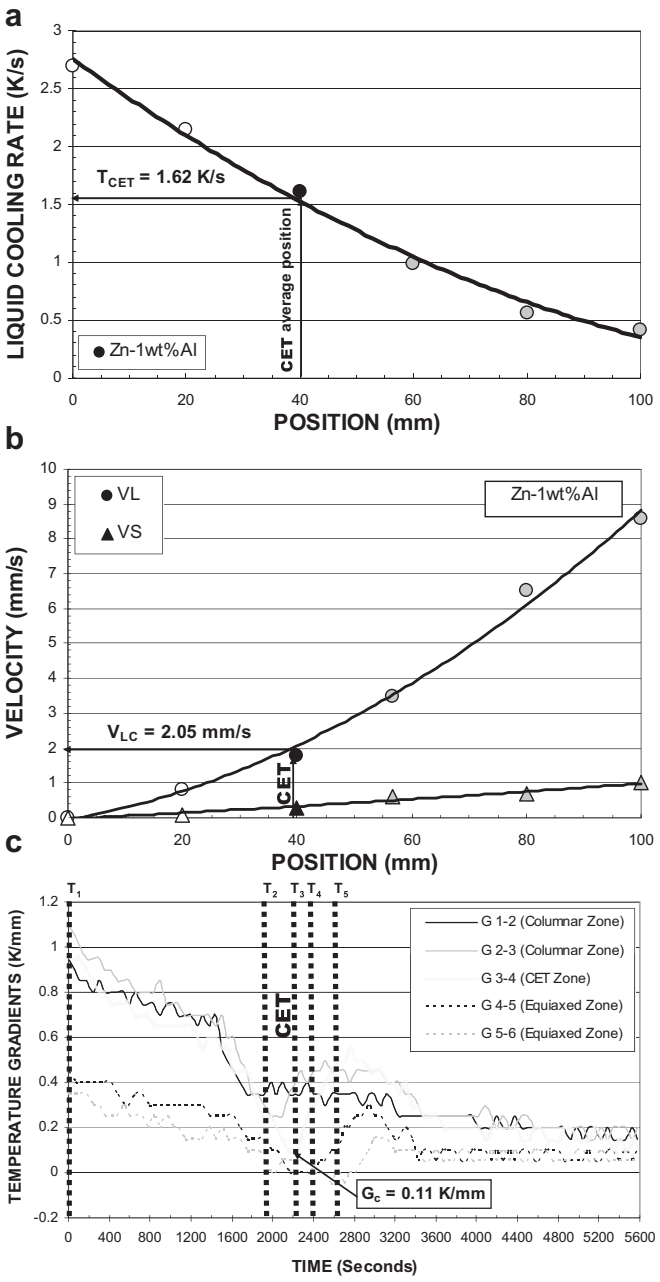

Fig. 7. (a) The liquid cooling rate versus distance from the end chill, (b) variation in V_L and V_S and (c) temperature gradients as a function of time during the end chill solidification test for one Zn-1wt%Al alloy.

selecting one sample of each region (equiaxed, columnar or cet) (see Fig. 3(a) and (b)). The pins were cut with a handsaw and then lathed at a slow velocity and low stress. One of the plane surfaces of the pin, which was ground and polished using SiC abrasive paper from #220 up to #1500 in grid size and then finished with 0.25 μm alumina suspensions, was used as the contact surface.

The disc axis was horizontally oriented and the pin was mounted vertically on top of the disc. A load of 32.4 N was applied on the pin axis [70]. The total distance and amount of wear were recorded during the test. The wear was measured by the change in length of the pin every 100–200 m of test up to a final distance of 2000 m. The final distance made sure that the steady state of wear was achieved in all the tests [66]. All the experiments were performed at room temperature and the ambient moisture ranged from 60 to 75% relative humidity.

The temperature of the samples was measured with a thermocouple inserted perpendicularly to the pin axis at 6 mm of the contact surface. In all the samples, the temperature at 6 mm of the surface was of 70 °C on average. The aspect of the pin after the wear test is presented in Fig. 3(d).

2.5. Corrosion tests

For corrosion testing, samples of 20 mm in length of each zone (columnar, equiaxed and CET) and for each concentration were prepared as working electrodes using the face which is parallel to the growth direction as active surface. This surface was polished with sandpaper (from CSi #200 to #1200) and washed with distilled water and dried by natural flow of air. The test electrodes of the different structures are shown in Fig. 4(a)

All the electrochemical tests were conducted in 3%NaCl solution (pH = 5.5) at room temperature (25 °C) using an IM6d Zahner® electrik potentiostat coupled to a frequency analyzer system.

A conventional three-compartment glass electrochemical cell, with its compartments separated by ceramic diaphragms, was used. The potential of the working electrode (area ≅ 20 mm^2) was measured against a saturated calomel reference electrode (0.242 V vs SHE), provided with a Luggin capillary tip. A large area Pt sheet was used as a counterelectrode. A scheme of the electrochemical device showing the position of the test electrode during the electrochemical tests is presented in Fig. 4(b)

Cyclic Voltammetry and Electrochemical Impedance Spectroscopy were used as the principal electrochemical techniques. Voltammograms were run at 25 °C between preset cathodic (open circuit potential ≈ −1.500 V) and anodic ($E_{s,a}$ = −0.700 V) switching potentials a potential sweep rate (v) of 0.002 V s^{-1}. Impedance spectra were recorded in the frequency range of 10^{-3}Hz ≤ f ≤ 10^5 Hz, at open circuit potential.

For comparison purposes, experiments using pure metals and aluminum-based alloys with different structures were conducted under the same experimental conditions.

3. Results and discussion

3.1. Columnar-to-equiaxed transition

Typical macro- and microstructures showing the columnar-to-equiaxed transition (CET) of the four alloy samples studied are presented in Fig. 2.

The position of the transition was located by visual observation and optical microscopy and the distance from the base of the sample was measured with a ruler. Fig. 2 shows that the CET is not sharp, showing a zone delimited by CET_{Max} and CET_{Min}, where some equiaxed grains co-exist with columnar grains. Normally, the size of the transition zone is in the order of up to 10 mm. Vanyoussefi and Greer [71] obtained a CET zone in Al-4.15wt%Mg alloys, whereas Gandin [72] and Ziv and Weinberg [8] found that the CET in their experiments was sharp.

3.2. Determination of solidification parameters

The temperature at five positions of each sample was measured by the inserted thermocouples and, as an example, a typical time-dependent temperature plot for the five thermocouples is shown in Fig. 5 for the Zn-1wt.%Al alloy. The distance from the chill and structure of each thermocouple position is indicated in the figure.

In all five curves it is possible to identify a period corresponding to the cooling of the melt, a second period of solidification, and

Table 2
Alloy system and observations of the calculations of thermal parameters at the CET during the directional solidification process.

Test N°	Alloys (wt%) and liquidus and solidus temperatures	Minimum CET position, $CET_{Min.}$ (mm)	Maximum CET position, $CET_{Max.}$ (mm)	Cooling rate in the melt, $\dot{T}_{CET}$, at the CET (K s^{-1})	Critical liquidus velocity, V_{LC} (mm s^{-1})	Critical temperature gradient, G_c (K mm^{-1})	Averages values of parameters for each composition
1	**Zn-1wt.%Al (ZA1)**	31.5 ± 0.1	47.1 ± 0.1	1.6 ± 0.2	2.1 ± 0.1	−0.00 ± 0.05	
2		58.6 ± 0.1	77.4 ± 0.1	2.3 ± 0.2	1.9 ± 0.1	0.11 ± 0.05	$CET_{Average}$ = 53.14 mm ± 0.1
3	$T_{Liquidus}$ = 689.8 K	49.4 ± 0.1	62.8 ± 0.1	2.2 ± 0.2	1.7 ± 0.1	−0.26 ± 0.05	$\dot{T}_{CET\ (Average)}$ = 2.09 K s^{-1} ± 0.2
4	$T_{Solidus}$ = 655 K	43.5 ± 0.1	50.5 ± 0.1	1.9 ± 0.2	1.9 ± 0.1	0.05 ± 0.05	$V_{L(Critical)}$ = 1.91 mm s^{-1} ± 0.1
5		51.0 ± 0.1	59.6 ± 0.1	2.2 ± 0.2	1.7 ± 0.1	−0.31 ± 0.05	$G_{L(Critical)}$ = −0.082 K mm^{-1} ± 0.05
6	**Zn-2wt.%Al (ZA2)**	53.9 ± 0.1	64.5 ± 0.1	2.3 ± 0.2	2.2 ± 0.1	−0.15 ± 0.05	
7		51.8 ± 0.1	76.1 ± 0.1	2.2 ± 0.2	1.9 ± 0.1	0.19 ± 0.05	$CET_{Average}$ = 52.57 mm ± 0.1
8	$T_{Liquidus}$ = 685.2 K	34.7 ± 0.1	48.9 ± 0.1	1.5 ± 0.2	1.5 ± 0.1	−0.23 ± 0.05	$\dot{T}_{CET\ (Average)}$ = 1.93 K s^{-1} ± 0.2
9	$T_{Solidus}$ = 655 K	42.3 ± 0.1	61.6 ± 0.1	1.8 ± 0.2	2.4 ± 0.1	−0.38 ± 0.05	$V_{L(Critical)}$ = 2.04 mm s^{-1} ± 0.1
10		39.6 ± 0.1	52.3 ± 0.1	1.6 ± 0.2	1.9 ± 0.1	−0.54 ± 0.05	$G_{L(Critical)}$ = −0.222 K mm^{-1} ± 0.05
11	**Zn-3wt.%Al (ZA3)**	34.7 ± 0.1	39.9 ± 0.1	1.7 ± 0.2	1.8 ± 0.1	−1.16 ± 0.05	
12		39.4 ± 0.1	43.6 ± 0.1	1.8 ± 0.2	2.0 ± 0.1	−0.83 ± 0.05	$CET_{Average}$ = 33.31 mm ± 0.1
13	$T_{Liquidus}$ = 671.2 K	31.8 ± 0.1	52.3 ± 0.1	1.5 ± 0.2	2.2 ± 0.1	−0.76 ± 0.05	$\dot{T}_{CET\ (Average)}$ = 1.59 K s^{-1} ± 0.2
14	$T_{Solidus}$ = 655 K	20.9 ± 0.1	34.3 ± 0.1	1.6 ± 0.2	2.0 ± 0.1	0.61 ± 0.05	$V_{L(Critical)}$ = 2.09 mm s^{-1} ± 0.1
15		12.7 ± 0.1	23.5 ± 0.1	1.1 ± 0.2	2.2 ± 0.1	−0.59 ± 0.05	$G_{L(Critical)}$ = −0.546 K mm^{-1} ± 0.05
16	**Zn-4wt.%Al (ZA4)**	23.9 ± 0.1	38.1 ± 0.1	1.6 ± 0.2	2.0 ± 0.1	−1.12 ± 0.05	
17		28.4 ± 0.1	39.2 ± 0.1	1.5 ± 0.2	2.1 ± 0.1	−0.91 ± 0.05	$CET_{Average}$ = 27.60 mm ± 0.1
18	$T_{Liquidus}$ = 663.5 K	17.3 ± 0.1	29.8 ± 0.1	1.3 ± 0.2	2.2 ± 0.1	−2.01 ± 0.05	$\dot{T}_{CET\ (Average)}$ = 1.44 K s^{-1} ± 0.2
19	$T_{Solidus}$ = 655 K	24.5 ± 0.1	33.6 ± 0.1	1.4 ± 0.2	2.3 ± 0.1	−1.29 ± 0.05	$V_{L(Critical)}$ = 2.16 mm s^{-1} ± 0.1
20		14.9 ± 0.1	26.3 ± 0.1	1.2 ± 0.2	2.0 ± 0.1	−0.36 ± 0.05	$G_{L(Critical)}$ = −1.138 K mm^{-1} ± 0.05

a final period of cooling of the solid to ambient temperature. Fig. 5 also shows the cooling rate of the melt, the temperature gradient in the liquid and the velocities of the isotherm fronts for both the liquidus and solidus temperatures.

The cooling rate ($\dot{T}$) was determined from the temperature versus time curves at each thermocouple position and taking the average slope of the temperature versus time curve during the cooling of the melt, before a period of solidification. The temperature interval used to calculate the average slope was between the *liquidus* temperature and the highest temperature above the *liquidus* reached by the melt before the furnace was turned off.

In the particular case of the interphase velocities, it is necessary to point out that in the present research we tracked the moving interphases using thermocouple measurements, and did not track dendrite tips, since temperature measurements were determined from a small volume and not from a surface. Temperature measurements were used to track averaged [$L/(S + L)$] interphases (or *liquidus* interphases) and [$(S + L)/S$] interphases (or *solidus* interphases) but not solid/liquid "interfaces", so dendrite tip surfaces, or equiaxed grain surfaces may be in any solid + liquid region [59]. We assumed that solid can not exist beyond the [$L/(S + L)$] interphase and that liquid can not exist beyond the [$(S + L)/S$] interphase. It is only into the mushy (solid + liquid) zone where all the "interfaces" do exist, and the mushy zone is at temperatures between the local liquidus temperature and the local solidus (or eutectic) temperature (see Fig. 6).

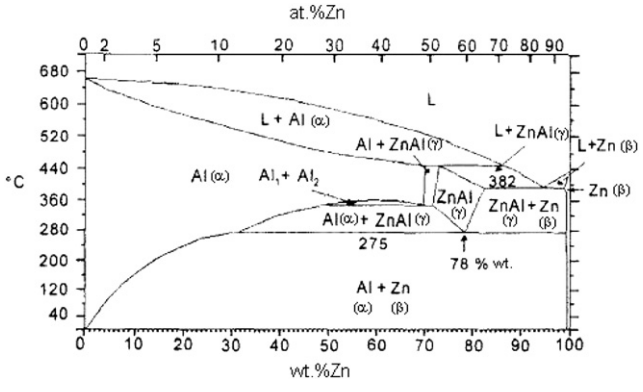

Fig. 8. Zn–Al phase diagram [69].

Each point in Fig. 7(a) corresponds to the liquid cooling rate value at each thermocouple position in the sample; the white points correspond to the values in the columnar zone, the black point to the CET zone and the gray points to the equiaxed zone.

The position of the solidification fronts versus time is determined by the start and the end of solidification at each thermocouple, which correspond to the liquidus and the solidus temperatures, respectively. Both points are detected by the changes in the slopes of the cooling curve at the start and end of solidification. The velocities of the solidification fronts were calculated as the distance between the thermocouples divided by the time taken by either the liquidus or solidus temperature to go from the lower to the upper thermocouple.

These velocities are denoted as VL and VS, respectively. The results are shown in Fig. 7(b). The origin of time in the figure corresponds to the initiation of solidification at the thermocouple of the bottom of the sample. We can see that the velocity of the liquid interphase (we did not measure the dendrite tip velocity) was zero at the beginning of solidification because all is in the liquid state. It can be noted that after 20 mm the liquid interphase advances very quickly. On the other hand, the solid front moves well behind the liquid front and accelerates much less than the liquid front.

The temperature gradient at all times was calculated by dividing the temperature difference between two thermocouples by the separation distance between them. The temperature gradients calculated from the readings of five thermocouples for Zn-1wt%Al are presented in Fig. 7(c), and referred to as G_{1-2}, G_{2-3}, G_{3-4}, G_{4-5} and G_{5-6}. The dashed vertical lines in the figure show the time at which the liquid isotherm reaches each thermocouple position; line T_1 coincides with the vertical axis and corresponds to the origin of the time axis.

It can be observed that the liquidus isotherm reaches the T_2 thermocouple position in 1980 s and the T_3 thermocouple position

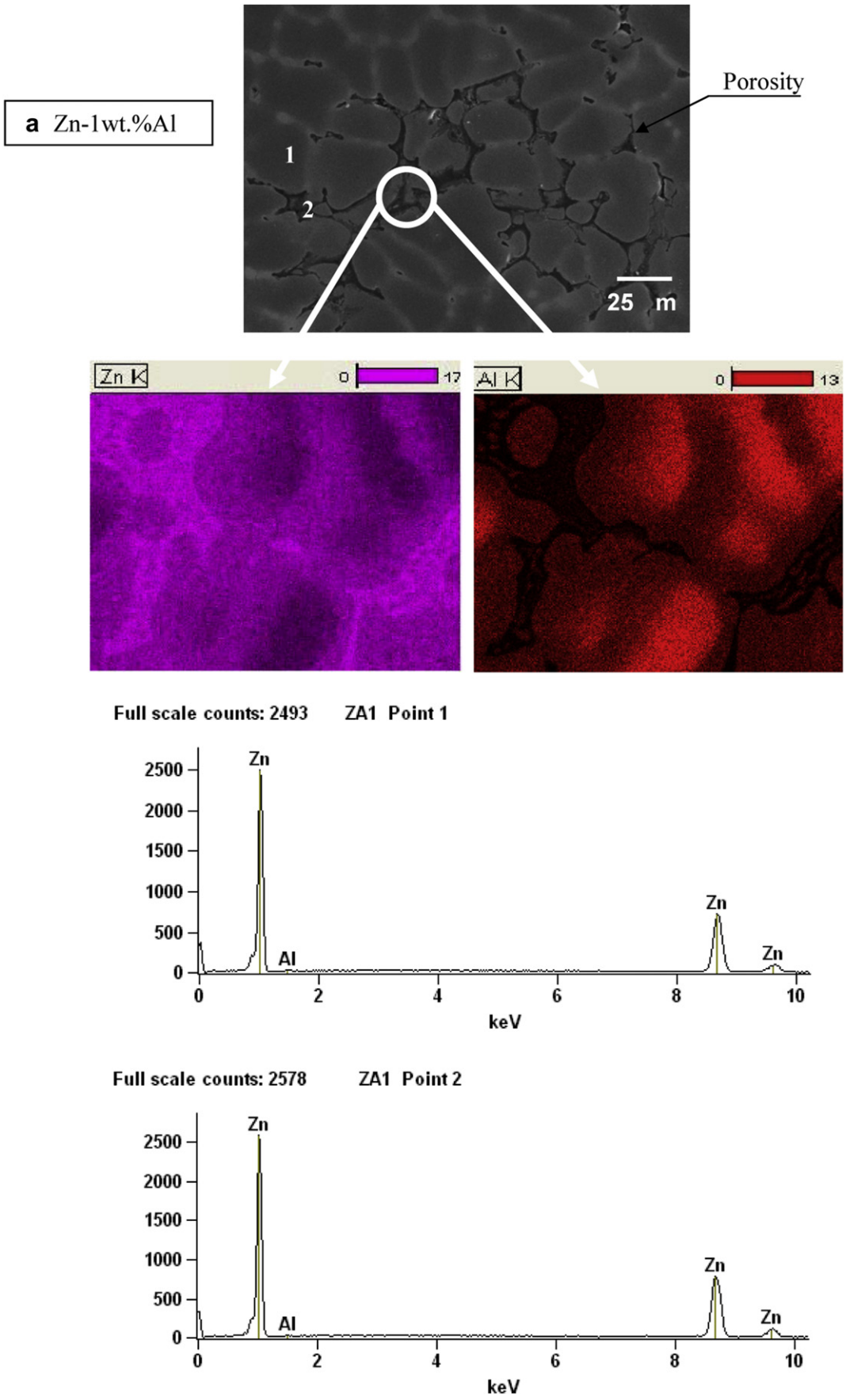

Fig. 9. SEM (Scanning Electron Microscopy) and EDXA (Energy Dispersive X-Ray Microanalysis) of Zn−Al alloys showing the distribution of elements. The Zn is distributed in the β dendrites and in the eutectic phase and α (Al) is present in the eutectic phase (α + β). Also, it is possible to see the typical morphology of hypoeutectic Zn−Al alloys: (a) Zn-1wt.%Al alloy showing the β (Zn) dendrites without the formation of interdendritic zone. Some porosity is present in these samples, as seen in the photograph. (b) Zn-2wt.%Al alloy and (c) Zn-3wt.%Al alloy showing the β (Zn) dendrites and a small interdendritic zone with eutectic formation. (d) Zn-4wt.%Al alloy showing the eutectic lamellar morphology (β + α).

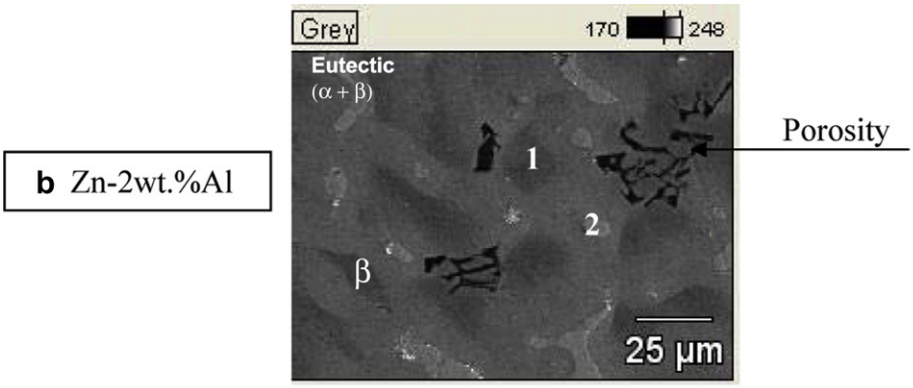

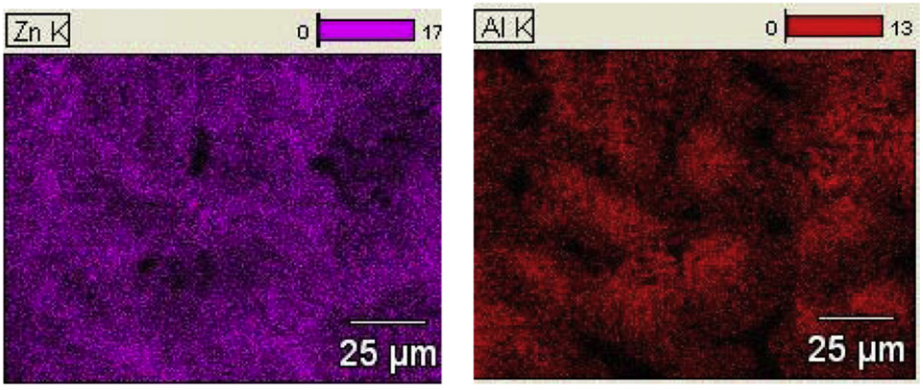

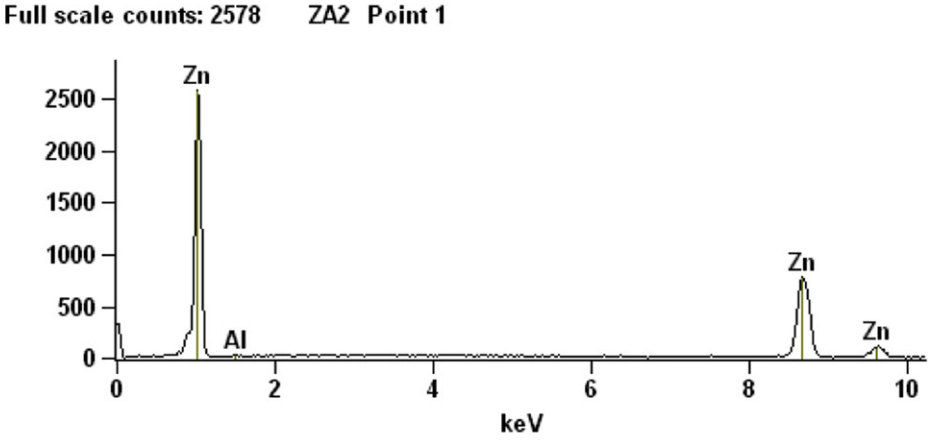

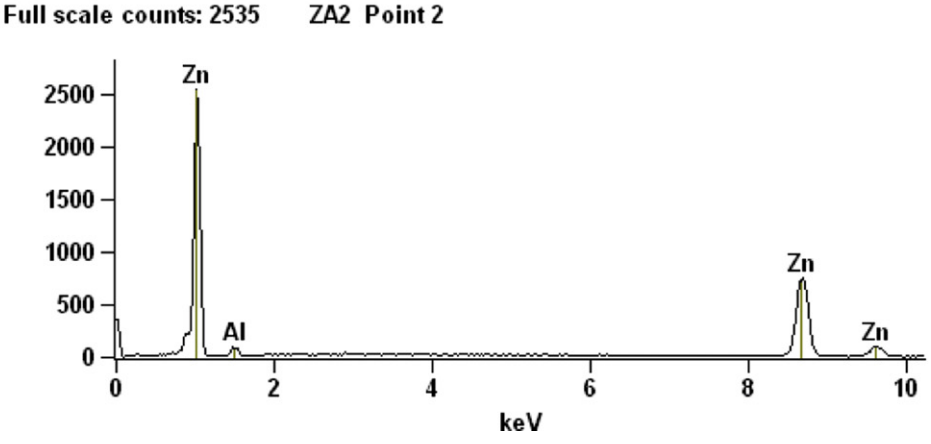

Fig. 9. (*continued*).

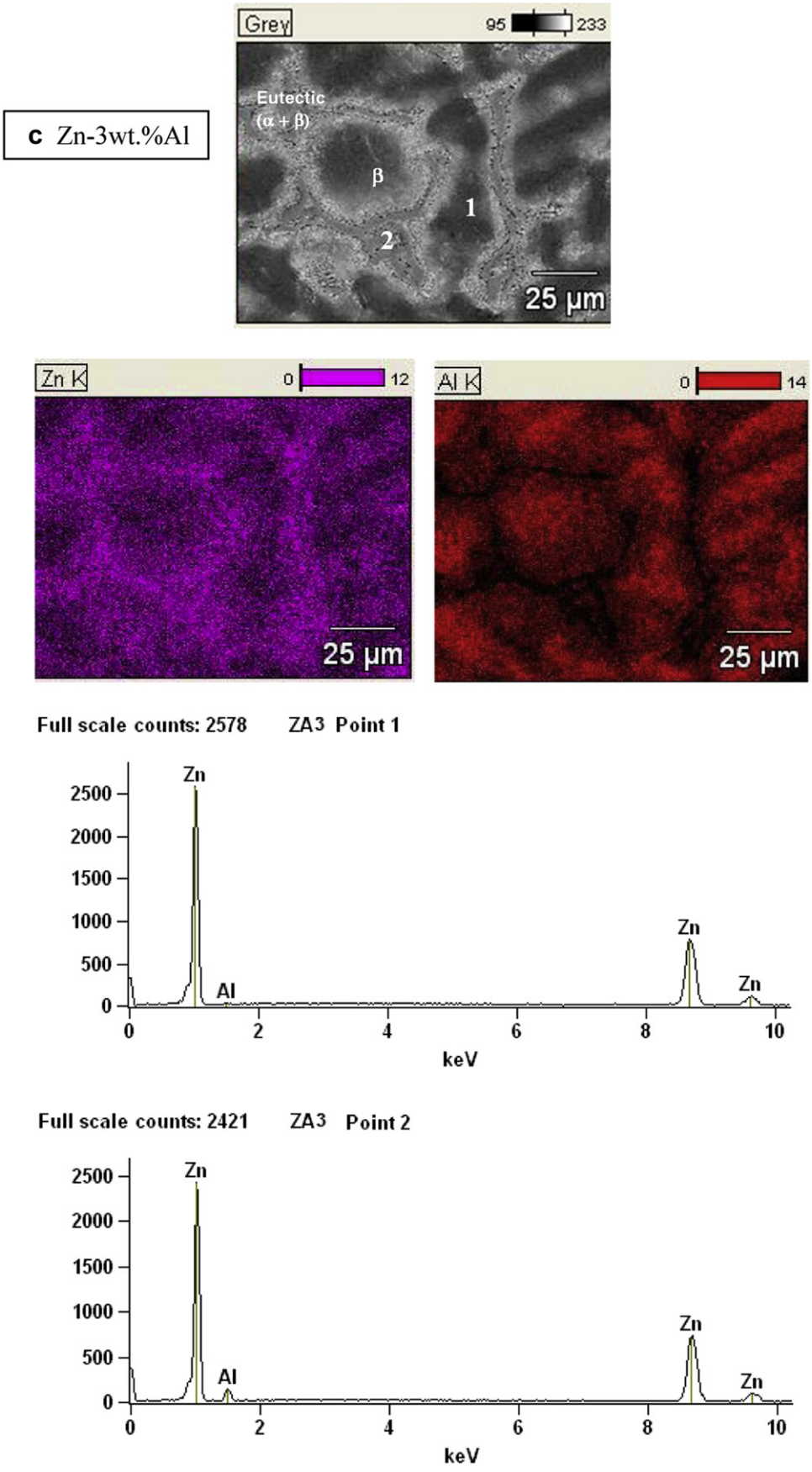

Fig. 9. (*continued*).

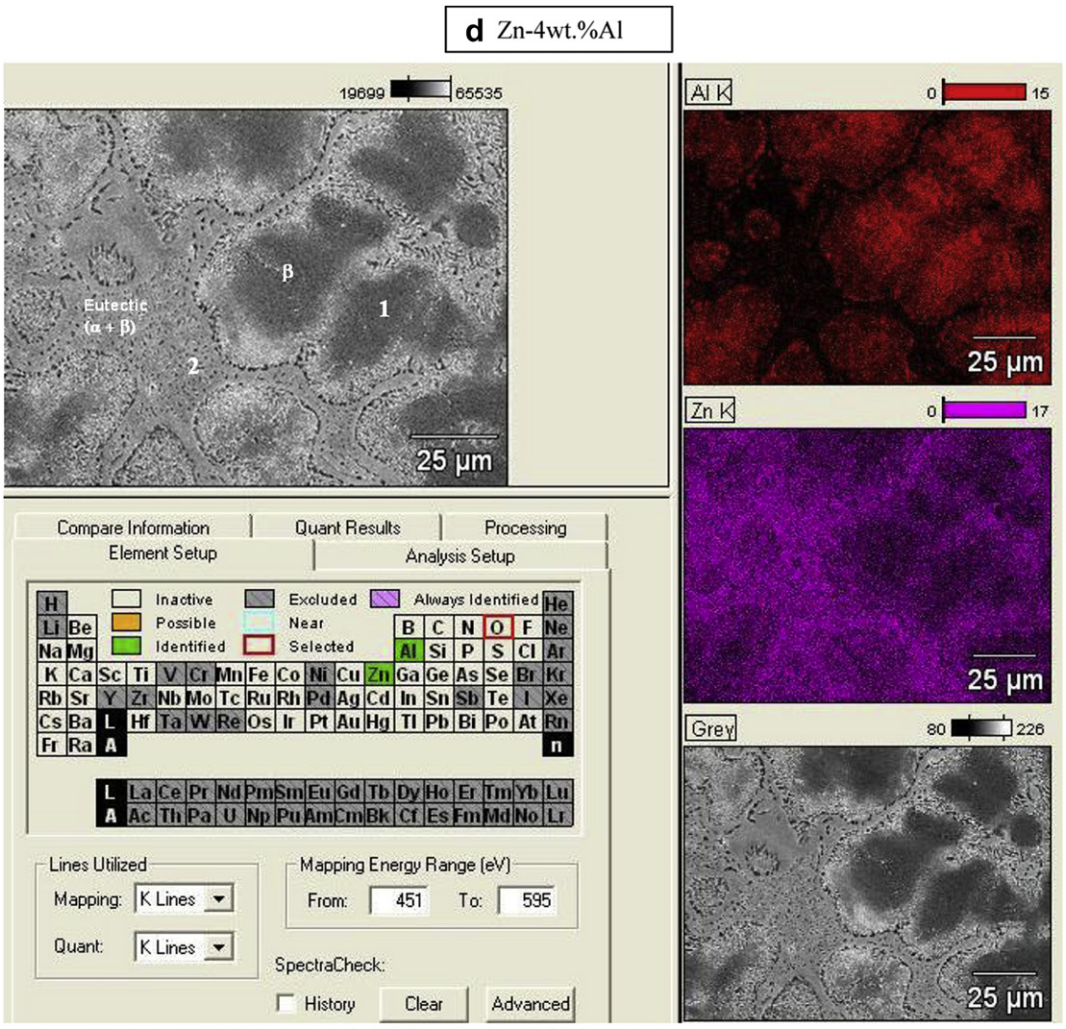

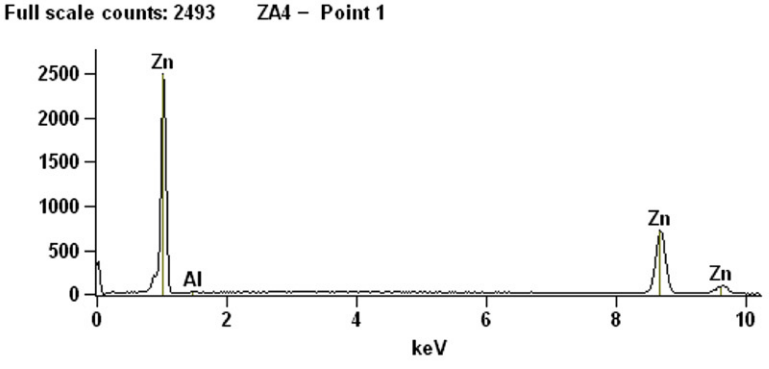

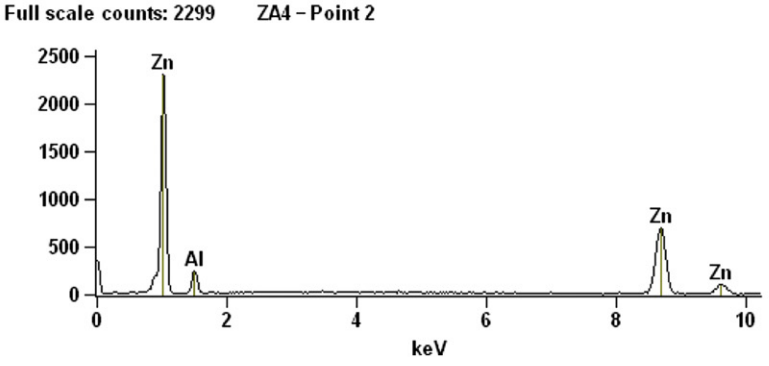

Fig. 9. (*continued*).

in 2260 s, which is the time when the transition at T_3 occurs. At the beginning, the gradients have values around 1 K mm^{-1} at the bottom of the sample, and 0.4 K mm^{-1} at the top. These values decrease gradually, when the transition occurs, and the gradient in the liquid becomes small, nearly to zero or slightly negative (about 0.1 K mm^{-1} in this specific case). This is the value of the critical temperature gradient, $G_{L(Critical)}$, for this experiment. This zero or slightly negative value of thermal gradient in the liquid at CET was first proposed by Ch.-A. Gandin [14] and also reported by us [13]. A similar behavior can be observed in all the samples. The critical temperature gradients for all the experiments are listed in Table 1.

The scatter in the values of gradient is associated with the fact that the transition usually occurs between two thermocouples and therefore, the calculated value is an average over a region which includes the mushy zone and the melt. In addition, according to the relative error presented above, at these low values of temperature differences, the error in the calculated gradients at these low values of temperature differences could be as large as 45%.

Thereby, taking these considerations into account, it can be concluded that within the error, the alloy composition does not have an effect on the temperature gradient during the transition.

Comparing the separation in time (x axis) between the dashed vertical lines in Fig. 7(c), which determines the time when the liquidus isotherm reaches the position of the corresponding thermocouple, it is observed that there are 1980 s between T_1 and T_2, 280 s between T_2 and T_3, 240 s between T_3 and T_4 and 120 s between T_4 and T_5. This shows that there is an acceleration of the liquidus interface and that the transition occurs not only at a low gradient but also with large interface velocities.

The most important thermal parameters extracted from the temperature versus time curves at the CET during the directional solidification process are listed in Table 2 for each hypoeutectic alloy.

3.3. Microstructures formed in hypoeutectic alloys during directional solidification

According to the Zn–Al phase diagram (Fig. 8) the phase formed at 418 °C is β (Zn) and liquid (L) up to 382 °C. Below this temperature, part of β (Zn) forms the γ phase (ZnAl) + β (Zn), up to 275 °C, when the eutectoid transformation γ (ZnAl) → α (Al) + β (Zn) occurs. Below 275 °C, β (primary, rich in Zn) + eutectoid (α + β) is formed. However, our directional solidification is a non-equilibrium solidification, and then high-temperature phases can be retained towards room temperature. Fig. 9(a) shows the microstructure of the Zn-1wt.%Al alloy, in the equiaxed zone, showing the β (Zn) dendrites without the formation of interdendritic zone.

In the case of the hypoeutectic alloys Zn-2wt.%Al, Zn-3wt.%Al and Zn-4wt.%Al, at approximately 416 °C, the β (Zn) phase + liquid (L) is formed up to 382 °C, when the eutectic transformation L → β (Zn) + γ (ZnAl) occurs. Below 382 °C, β (Zn) phase + Eutectic (β (Zn) + γ (ZnAl)) is formed up to 275 °C, when the eutectic transformation γ (ZnAl) → α (Al) + β (Zn) occurs. Below 275 °C, the β (primary, rich in Zn) + eutectoid (α + β) is formed.

From Zn-2%wt.Al to Zn-4%wt.Al alloys, the eutectic phase (interdendritic region) formed increases at expense of the β (Zn), with $k = C_S/C_L = 0.20$ (see Table 3 and Fig. 9b–d

3.4. Evolution of structural parameters with directional solidification

The typical EDXA micrograph of the hypoeutectic and hypereutectic Zn–Al alloys studied is presented in Fig. 9. From Zn-2wt%Al (Fig. 9(b)) to Zn-4wt.%Al (Fig. 9(c)) it is possible to observe that the dendritic matrix is Zn-rich (β phase) whereas the interdendritic region, which is the eutectic (α + β) phase, is Al-rich.

We carefully analyzed the microstructures of all the samples using EDXA and found no evidence of the presence of the discontinuous precipitation (DC) phenomenon in the samples, at room temperature and along the time during which the experiments were performed [49–58]. The presence of porosity was observed in some samples, as seen in Fig. 9(a).

Fig. 10 shows the evolution of the secondary dendrite arm spacing (λ_2) as a function of the distance from the caloric extraction surface (bottom of the sample) for all the hypoeutectic alloys studied (Zn-1wt%Al, Zn-2wt%Al, Zn-3wt%Al and Zn-4wt%Al). It is possible to see that λ_2 increases from the columnar to equiaxed zone of the samples, because the heat extraction and cooling rate are higher during columnar than during equiaxed growth, producing a shorter solidification time.

It is also observed that λ_2 decreases from 1wt%Al to 4wt%Al alloys, which is expected for the higher increase in the solute at dendrite interface arms, which is predicted by models [73]. In addition, there might be a difference in the solidification time between both experiments. The values of λ_2 versus position (P, distance from the bottom) are fitted by $\lambda_2 = a.P^b$, where the value of parameter a decreases from 38.33 (Zn-1wt%Al) to 14.43 (Zn-4wt%Al) and the value of b increases from 0.16 (Zn-1wt%Al) to 0.26 (Zn-4wt%Al), see Table 5.

The evolution of grain size with distance from the bottom of the sample is presented in Fig. 11.

The size of the equiaxed grains for the Zn-1wt%Al sample is 1.5 mm in the transition region and then starts to monotonically increase up to a value of 4.5 mm at the end of the sample. In the case of the width of the columnar grains, it is observed that the size increases from 2 mm in whole columnar zone to 3.8 mm at the end of the transition region. A similar analysis was performed for all solidification experiments, as shown in Fig. 11 for other alloy concentrations (the equiaxed points in the figures were fitted to polynomial functions of third degree). It is observed that in the transition region, the size of the equiaxed grains is smaller than the width of the columnar grains (the black points in the figures correspond to the measurements of the size of the columnar and equiaxed dendrites in the CET zone). However, in all cases, the size increases after the transition. At the end of solidification, the size of equiaxed grains also reaches a maximum value.

The figures show that the grain size in the Zn-2wt%Al sample increases from 1.8 mm to 2.7 mm in the columnar zone and from 1.4 mm to 3.8 mm in the equiaxed zone. In the Zn-3wt%Al alloy, the grain size is between 1.7 mm and 2.7 mm in the columnar area and between 1.2 mm and 3.5 mm in the equiaxed area. Finally, for the Zn-4wt%Al alloy, the size increases from 1.3 mm to 3.2 mm (columnar zone) and from 0.8 mm to 2.2 mm (equiaxed zone). The size of the grains in the three regions (columnar, equiaxed and CET) decreases from the Zn-1wt%Al to the Zn-4wt%Al alloy.

The values of grain size (G_S) versus position (P) are fitted by $G_S = c.P^d$. For the columnar zones, the value of c varies from 1.17 (Zn-1wt%Al) to 0.79 (Zn-4wt%Al) and the value of d increases from 0.25 (Zn-2wt%Al) to 0.31 (Zn-4wt%Al), whereas for the equiaxed zones the value of c increases from 0.01 (Zn-1wt%Al) to 0.12 (Zn-4wt%Al) and the value of d decreases from 1.27 (Zn-2wt%Al) to 0.58 (Zn-4wt%Al), see Table 6.

The evolution of λ_2 with G_S is shown in Fig. 12 for all alloy concentrations. In both cases, when the grain size increases, λ_2 increases as well in the columnar and equiaxed zones of the samples. The values of both λ_2 and grain size of columnar grains in the area of the CET are usually larger or approximately equal to the size in the equiaxed zone.

Table 3
Solid and liquid fractions of hypoeutectic Zn–Al alloys.

Hypoeutectic Zn–Al alloy	f_s (Dendritic region)	f_l (Interdendritic region)
Zn-1% wt.Al	87%	13%
Zn-2%wt.Al	68%	32%
Zn-3% wt.Al	47%	53%
Zn-4%wt.Al	25%	75%

It is observed that there is a relation that indicates that the grain size increases as λ_2 increases in both the columnar and equiaxed regions. However, as shown in Fig. 12, the relation is different in each zone, showing that a given grain size in the columnar zone is formed with dendrites of smaller λ_2 than in the equiaxed zone. It is necessary to mention that what is reported as grain size in the columnar zone is actually the columnar width. Also, the local solidification time is higher in the CET and equiaxed zones than in the columnar zone (see Fig. 5), contributing to the increase in grain size and dendrite spacing in the equiaxed zone.

The values of secondary λ_2 versus grain size (G_S) are fitted by $\lambda_2 = e.G_S^f$. For the equiaxed zones, the value of e decreases from 69.45 (Zn-1wt.%Al) to 36.95 (Zn-4wt.%Al) and the value of f increases from 0.10 (Zn-1wt.%Al) to 0.45 (Zn-4wt.%Al), whereas for the columnar zones, the value of e decreases from 35.47 (Zn-1wt.% Al) to 17.78 (Zn-4wt.%Al) and the value of f increases from 0.49 (Zn-21wt.%Al) to 0.91 (Zn-4wt%Al), see Table 7.

3.5. Corrosion resistance of different alloys and structures

3.5.1. Voltammetric data

Fig. 13 shows the voltammograms of the columnar and equiaxed zinc (Fig. 13(a)) and of different hypoeutectic alloys and structures, that is, columnar, CET and equiaxed (Fig. 13b–d) In all the cases, it is possible to observe that during the anodic potential scanning the current is practically zero until it reaches the potential of −1 V, when the current increases sharply, thus beginning the active dissolution of metal. The voltammetric curves in the backward direction show a hysteresis loop, suggesting that this current increase was due to the start of a process of pitting. Two cathodic current peaks at about −1.2 V and −1.3 V (called C_1 and C_2, respectively) for the equiaxed structure in Fig. 13(a)) are also present, which could be associated with the reduction of ZnO and $Zn(OH)_2$ [37]. In the case of columnar structure only one C_1 peak corresponding to ZnO is observed.

Table 4
Values of the Electrochemical Impedance Spectroscopy (EIS) adjusting parameters for each structure and alloy concentration.

Alloy and type of structure	R_{ct} (Ω cm^2)	C (F cm^{-2})
Zn $_{Columnar}$	414	$6.4 \times 10^{-06} \pm 1*10^{-7}$
Zn $_{CET}$	401	$3.8 \times 10^{-06} \pm 1*10^{-7}$
Zn $_{Equiaxed}$	384	$2.8 \times 10^{-06} \pm 1*10^{-7}$
Al $_{Columnar}$	19	$3.3 \times 10^{-06} \pm 1*10^{-7}$
Al $_{CET}$	15	$1.7 \times 10^{-05} \pm 1*10^{-6}$
Al $_{Equiaxed}$	11	$2.7 \times 10^{-04} \pm 1*10^{-5}$
Zn-1wt.%Al $_{Columnar}$	983 ± 10	$1.9 \times 10^{-5} \pm 1*10^{-6}$
Zn-1wt.%Al $_{CET}$	358 ± 10	$3.0 \times 10^{-4} \pm 1*10^{-5}$
Zn-1wt.%Al $_{Equiaxed}$	310 ± 10	$2.4*10^{-4} \pm 1*10^{-5}$
Zn-2wt.%Al $_{Columnar}$	800 ± 10	$1*10^{-4} \pm 1*10^{-5}$
Zn-2wt.%Al $_{CET}$	503 ± 10	$2.4*10^{-4} \pm 1*10^{-5}$
Zn-2wt.%Al $_{Equiaxed}$	300 ± 10	$3.2 \times 10^{-4} \pm 1*10^{-5}$
Zn-3wt.%Al $_{Columnar}$	590 ± 10	$1.3*10^{-4} \pm 1*10^{-5}$
Zn-3wt.%Al $_{CET}$	390 ± 10	$2.1*10^{-4} \pm 1*10^{-5}$
Zn-3wt.%Al $_{Equiaxed}$	234 ± 10	$3.6 \times 10^{-4} \pm 1*10^{-5}$
Zn-4wt.%Al $_{Columnar}$	351 ± 10	$8.6 \times 10^{-4} \pm 1*10^{-5}$
Zn-4wt.%Al $_{CET}$	345 ± 10	$1.1*10^{-4} \pm 1*10^{-4}$
Zn-4wt.%Al $_{Equiaxed}$	180 ± 10	$1.7*10^{-3} \pm 1*10^{-4}$

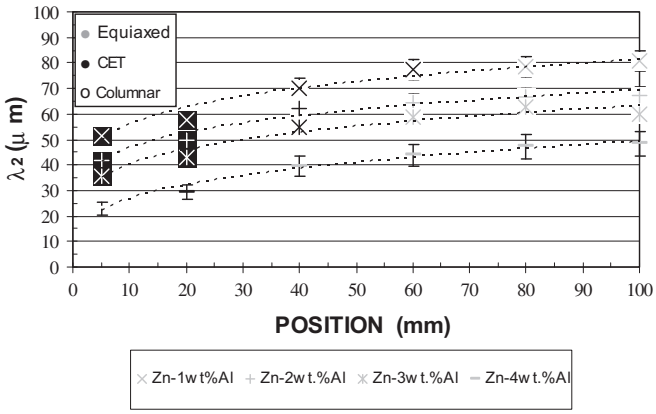

Fig. 10. Grain size experimentally measured as a function of distance from the bottom of the samples.

As the concentration of aluminum in the alloy increases, the definition of these peaks of reduction is not clear, although the C_2 peak is dominant. The most important difference is observed in the distribution of the cathodic current peaks, which indicates the different characteristics of the films formed during the anodic scan. These results can be attributed to the aggressive/depassivating action of Cl^- anions [74]. At present, the mechanism of film formation is still uncertain.

For the case of CET, profiles are more complex, because the proportion of one or other type of grains (columnar or equiaxed) can vary from sample to sample (Fig. 13(c)).

For the equiaxed structures and for more diluted alloys (Zn-1wt.%Al) the reduction current decreases to about half, indicating that the passive layer formed on the material is more protective (Fig. 13(d)).

In the alloys, the values of the currents are similar for the same Al concentration and the most important difference is observed in the cathodic current peaks, which indicates the different characteristics of the films formed during the anodic scan. As it is known, the aluminum corrosion products are more insulated than those of zinc.

The orientation of the grains in a polycrystalline zinc alloy has preferential orientations depending on the casting process and the mechanical working conditions. For example, in the case of cast products the <0001> direction is perpendicular to the axis of the cast columnar crystals [75]. Thus, in the columnar sections, the grains grow in more favorable directions to promote the formation of a film with more protective characteristics.

This different contribution of the peaks in the voltammograms gives rise to surface layers with different corrosion products, where samples with 4wt.%Al show the formation of a thicker layer of corrosion products (see Fig. 14a–d for Zn-1wt.%Al, Zn-2wt.%Al, Zn-3wt.%Al and Zn-4wt.%Al respectively).

3.5.2. Electrochemical impedance spectroscopy data

Impedance spectra are dependent on the composition and structures of the alloys. The experimental Nyquist diagrams of the

Table 5
λ_2 versus position (P) fitted by $\lambda_2 = a.P^b$: values of a and b for different alloys and structures.

Alloy	λ_2 versus position	R^2
Zn-1wt.%Al	$\lambda_2 = 38.33.P^{0.1628}$	0.9448
Zn-2wt.%Al	$\lambda_2 = 31.33.P^{0.1718}$	0.9682
Zn-3wt.%Al	$\lambda_2 = 25.44.P^{0.1971}$	0.9530
Zn-4wt.%Al	$\lambda_2 = 14.43.P^{0.2660}$	0.9773

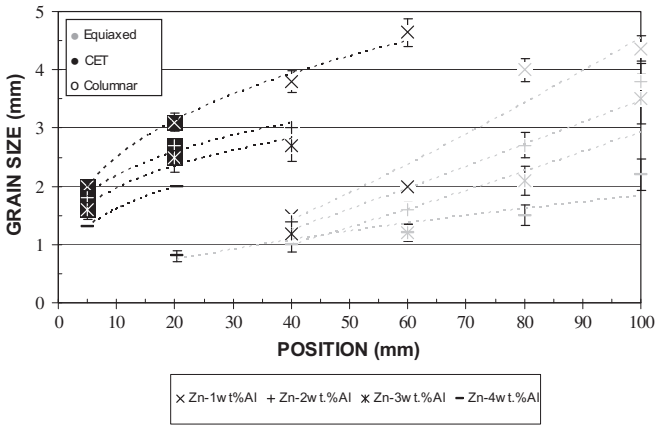

Fig. 11. Secondary dendritic arm spacing versus grain size in different zones of the samples.

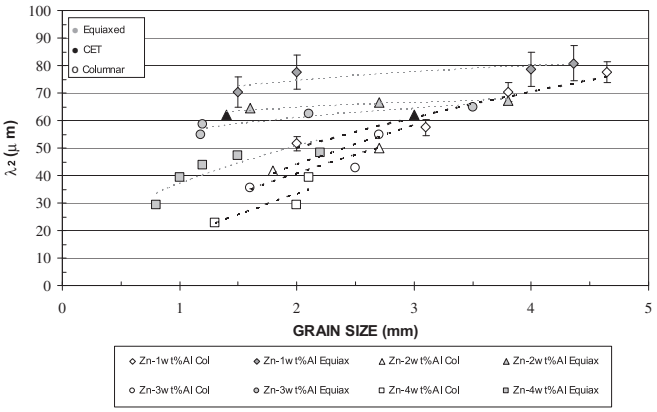

Fig. 12. Secondary dendrite arm spacing (λ_2) versus grain size in different zones of the samples.

Zn-1wt%Al, Zn-2wt%Al, Zn-3wt%Al and Zn-4wt%Al alloys for the different structures are presented in Fig. 15a–d respectively. The diagrams show one capacitive time constant at high and intermediate frequencies and a not well-defined time constant at low frequencies.

For the Zn-1wt.%Al, Zn-2wt.%Al and Zn-3wt.%Al alloys, the impedance values depend on the alloy structure and only for the equiaxed sample, the capacitive loop at high frequencies is well defined. On the other hand, as the Al concentration increases to 4wt.%Al, the impedance data are similar for all the structures.

The whole set of experimental impedance spectra can be discussed according to the following total transfer function, corresponding to the circuit of Fig. 16:

$$Z_t(jw) = R_\Omega + Z \tag{1}$$

with:

$$\frac{1}{Z} = \frac{1}{R_{ct} + Z_W} + j.w.C \tag{2}$$

where $R\Omega$ is the ohmic solution resistance, $\omega = 2\pi f$; C_{dl} the capacitance of the electric double layer, R_{ct} the charge transfer resistance and Z_W the diffusion contributions in impedance spectra.

The good agreement between the experimental and simulated data according to the transfer function given in the analysis of Eqs. (1) and (2) using non-linear least square fit routines is demonstrated in Fig. 17 for the Zn-1wt.%Al alloy (CET structure). The values of C and R_{ct} determined from the optimum fit procedure are presented in Table 4.

The analysis of the impedance parameters associated with the time constant at low frequencies is difficult because it is incomplete in some cases. However, it was possible to calculate an approximate value of diffusion coefficient $D \approx 10^{-10}$–10^{-12} cm^2 s^{-1} from the fitting.

The corrosion current can be related to the R_{ct} in the case of mixed control [76], where the polarization resistance technique fails, according to the following expression:

$$R_{ct} = b_a.b_c/[2.303.(b_a + b_c).I_{corr}] \tag{3}$$

The experimental data shown in Table 4 indicate that the values of R_{ct} decrease from columnar to equiaxed structures and from 1wt.%Al to 4wt.%Al alloys. These results indicate that when the aluminum concentration increases in the interdendritic region (eutectic lamellar mixture) the susceptibility to corrosion increases and the effect is more notorious for the equiaxed structure.

Furthermore, the R_{ct} values are related to the rate of charge transfer reactions that give rise to the formation of a corrosion layer on the surface of the samples but say nothing about the protective characteristics of the film formed. The double-layer capacitance, C_{dl}, gives us this information. Table 4 shows that C_{dl} increases from Zn-1wt.%Al to Zn-4wt.%Al alloys. The high values of C_{dl} in the case of Zn-4wt.%Al alloys with equiaxed structure confirm the formation of porous corrosion products (Fig. 14(d)), as determined by other authors by X-ray diffraction [77].

3.6. Microhardness

The Vickers microhardness of four different alloys versus position with respect to the chill is plotted in Fig. 18. It can be seen that Vickers microhardness increases from the columnar to equiaxed zones of the samples as well as with the increase in aluminum content in the samples.

The directional solidification process creates gradients of composition along the length of the material. This, in turn, may

Table 6
Grain size (G_S) versus position (P) fitted by $G_S = c.P^d$: values of c and d for different alloys and structures.

Alloy	Grain size versus position	R^2
Zn-1wt.%Al $_{Columnar}$	$G_S = 1.166.P^{0.3292}$	0.9939
Zn-1wt.%Al $_{Equiaxed}$	$G_S = 0.012.P^{1.2732}$	0.9285
Zn-2wt.%Al $_{Columnar}$	$G_S = 1.216.P^{0.2523}$	0.9814
Zn-2wt.%Al $_{Equiaxed}$	$G_S = 0.020.P^{1.1145}$	0.9024
Zn-3wt.%Al $_{Columnar}$	$G_S = 1.072.P^{0.2617}$	0.9618
Zn-3wt.%Al $_{Equiaxed}$	$G_S = 0.013.P^{1.1664}$	0.8038
Zn-4wt.%Al $_{Columnar}$	$G_S = 0.792.P^{0.3074}$	1
Zn-4wt.%Al $_{Equiaxed}$	$G_S = 0.127.P^{0.58}$	0.8851

Table 7
Secondary spacing (λ_2) versus grain size (G_S) fitted by $\lambda_2 = e.G_S^f$: values of e and f for different alloys and structures.

Alloy	λ_2 versus grain size	R^2
Zn-1wt.%Al$_{Columnar}$	$\lambda_2 = 35.467.G_S^{0.4953}$	0.9226
Zn-1wt.%Al$_{Equiaxed}$	$\lambda_2 = 69.446.G_S^{0.101}$	0.7534
Zn-2wt.%Al$_{Columnar}$	$\lambda_2 = 27.242.G_S^{0.6921}$	0.8664
Zn-2wt.%Al$_{Equiaxed}$	$\lambda_2 = 61.496.G_S^{0.0716}$	0.8613
Zn-3wt.%Al$_{Columnar}$	$\lambda_2 = 25.308.G_S^{0.6879}$	0.8541
Zn-3wt.%Al$_{Equiaxed}$	$\lambda_2 = 55.591.G_S^{0.133}$	0.8339
Zn-4wt.%Al$_{Columnar}$	$\lambda_2 = 17.778.G_S^{0.9144}$	0.7895
Zn-4wt.%Al$_{Equiaxed}$	$\lambda_2 = 36.953.G_S^{0.4548}$	0.7571

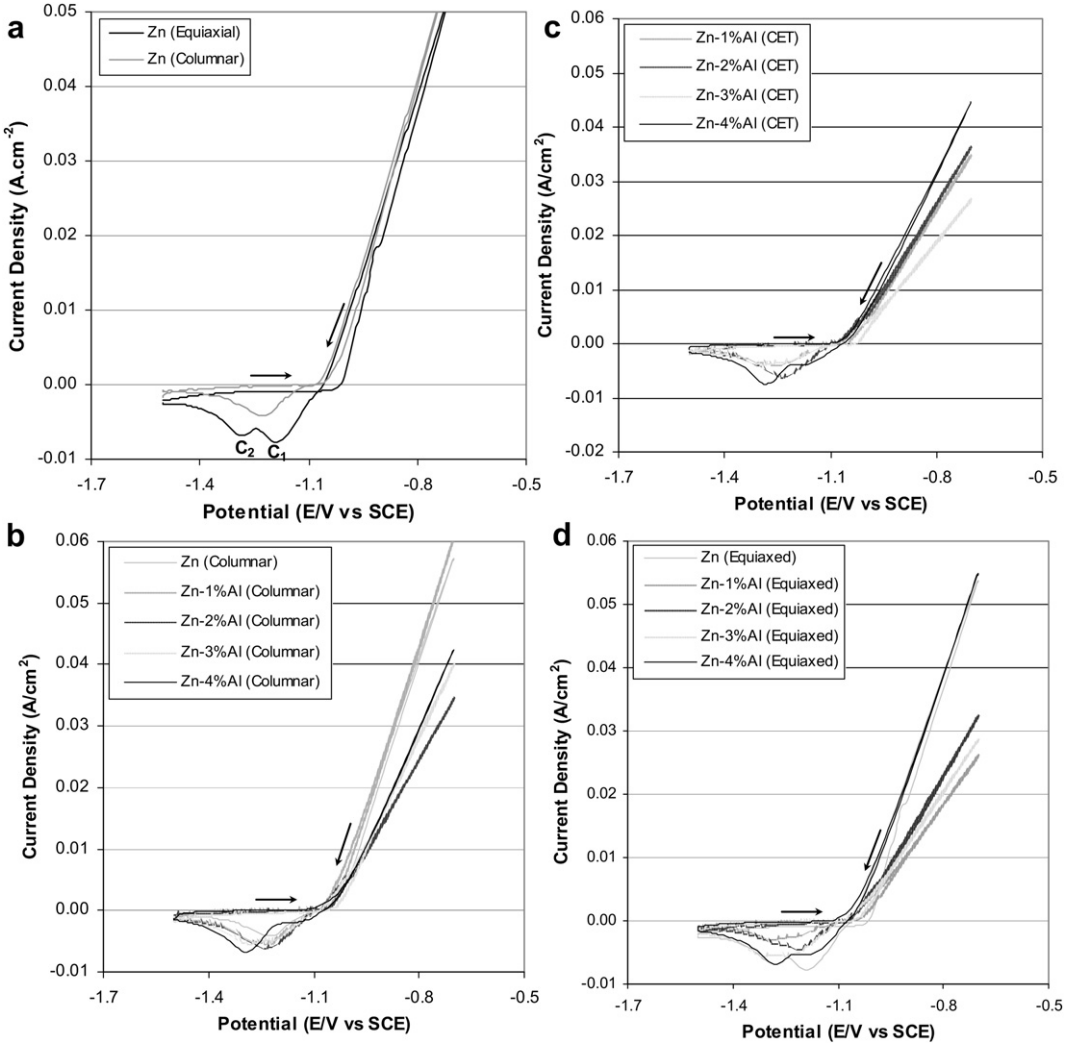

Fig. 13. Voltammograms of (a) Zn equiaxed and (b–d) Zn–Al diluted alloys with different structures: (b) columnar (c) CET and (d) equiaxed.

affect the hardness and, consequently, the wear resistance. The composition of the different alloying elements along the cast samples was analyzed by Scanning Electron Microscopy (SEM) and Energy Dispersive X-Ray Microanalysis (EDXA) and some results are shown in Fig. 19a–d.

In the macroscale, the aluminum concentration increases in the direction of solidification from the bottom to the top of the samples. We found that the silicon concentration also increases but that the iron composition decreases in the direction of solidification. The increase in Si is more pronounced with the increase in aluminum concentration in the alloy, which could explain the increase in microhardness in the case of Zn-4wt.%Al in the CET and equiaxed zones with respect to the other alloys with lower concentrations of Al (Fig. 19).

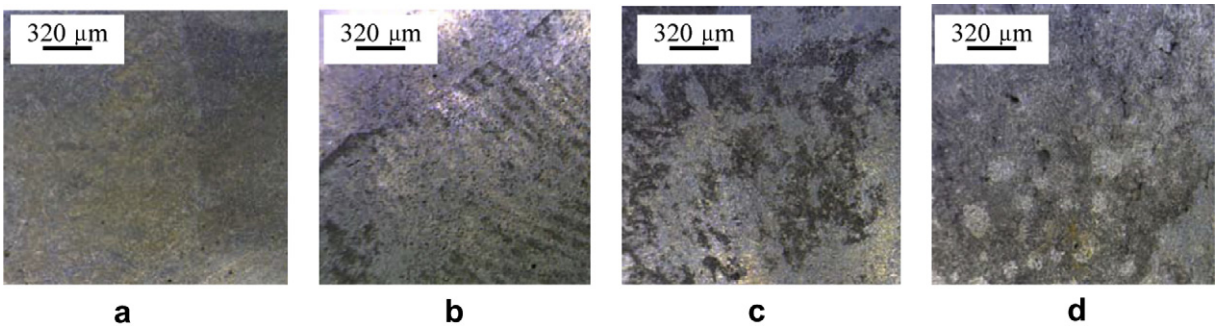

Fig. 14. Micrographs showing the formation of corrosion products on the surface of different samples with equiaxed structure, after the cyclic voltammetry test. (a) Zn-1wt.%Al, (b) Zn-2wt.%Al, (c) Zn-3wt.%Al and (d) Zn-4wt.%Al.

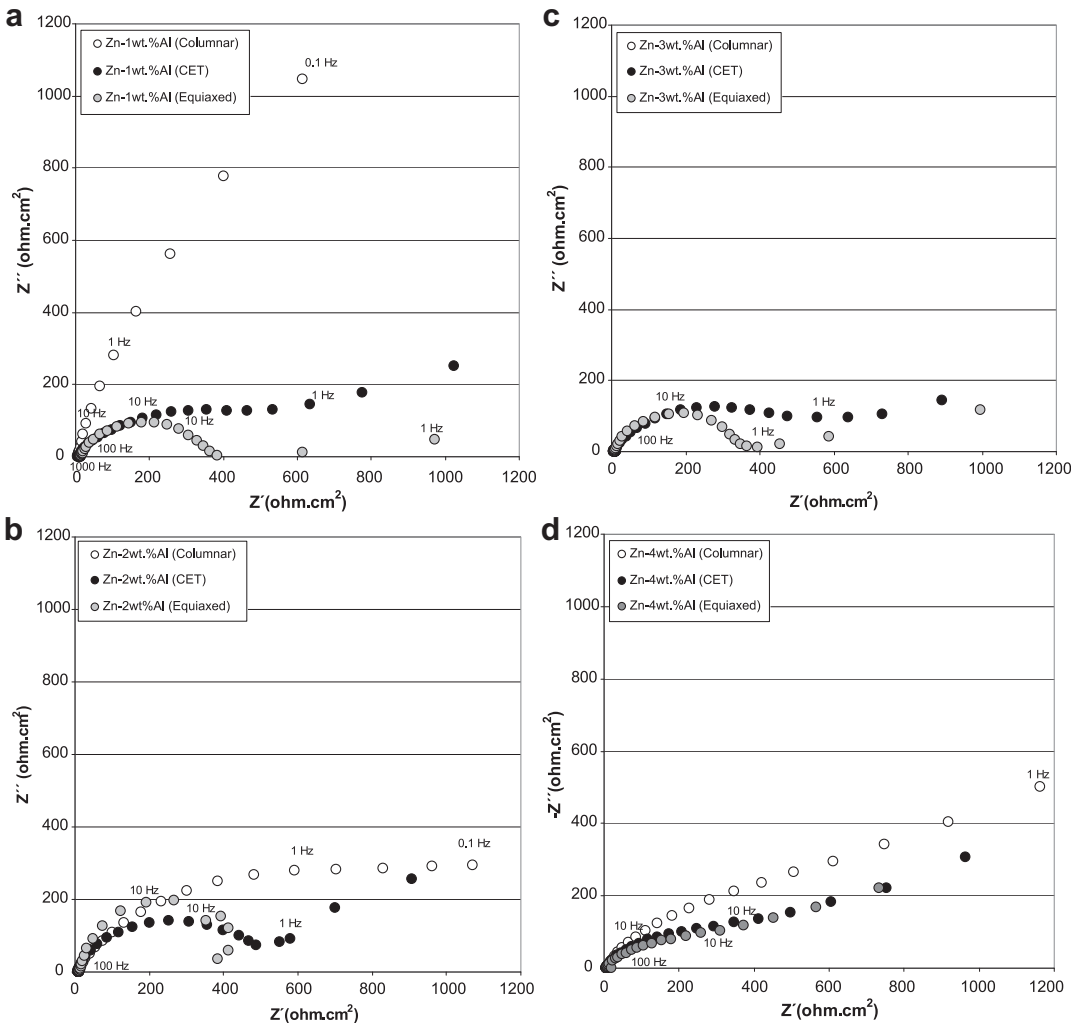

Fig. 15. Nyquist of (a) Zn-1wt.%Al, (b) Zn-2wt.%Al, (c) Zn-3wt.%Al and (d) Zn-4wt.%Al alloys with different grain structures.

3.7. Wear resistance

The results of the wear rate as a function of Zn–Al alloys with different structures and composition are shown in Fig. 20. From these results it is possible to calculate the wear resistance as the mathematical inverse of the wear rate.

It is observed that the wear rate of the equiaxed structure is lower than that of the columnar structure. When analyzing the influence of the aluminum composition on the wear rate independently of the structure it is observed that as the aluminum concentration increases, the wear rate decreases.

The gray lines plotted in Fig. 20 show the influence of aluminum concentration by type of structure. The dark gray line indicates the

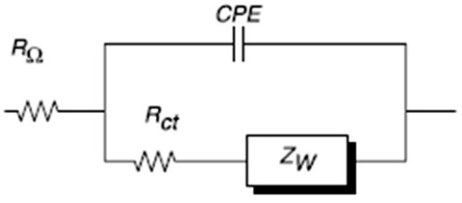

Fig. 16. Equivalent circuit corresponding to the transfer functions given by Eq. (2).

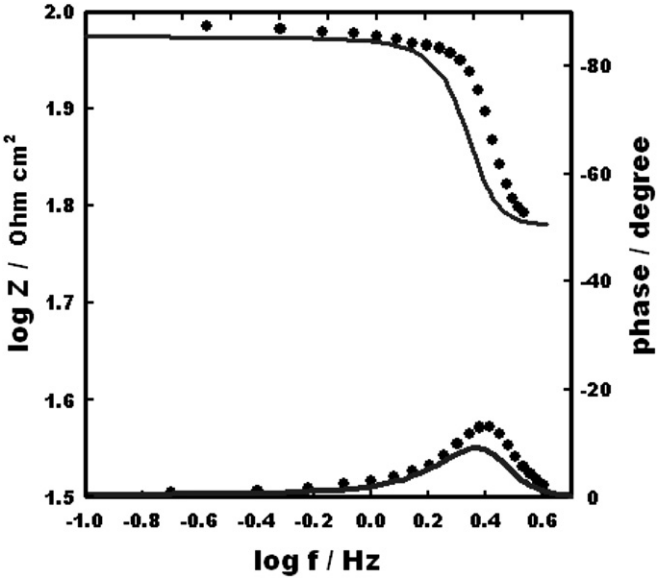

Fig. 17. Bode diagram for Zn-4wt%Al indicating the experimental data (…) and the fitted values (—).

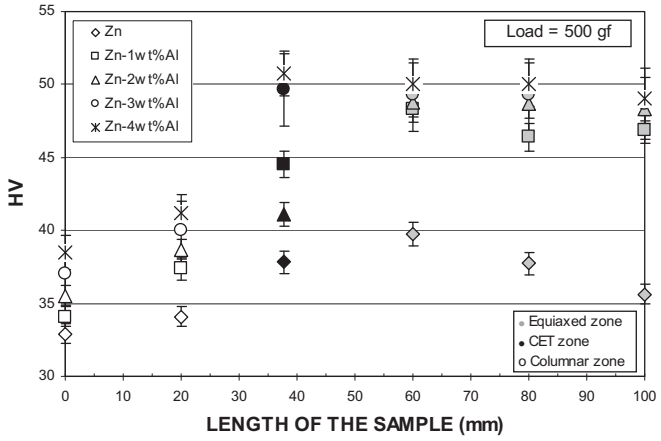

Fig. 18. Microhardness values versus length of Zn–Al alloy samples using a load of 500 g_f.

wear rate of the equiaxed structure whereas the light gray line indicates the wear rate of the columnar structure.

The wear rate of the equiaxed structure decreases from 1.15 x 10^{-3} mm m^{-1} to a constant value of 4 x 10^{-4} mm m^{-1} when the aluminum concentration increases from 0 to 2wt.%Al, and it is the same value up to 4wt.%Al. On the other hand, for the columnar structure, the wear rate is constant for an aluminum concentration lower than 3 wt.%, with a value of approximately 1.5 x 10^{-3} mm m^{-1}, and at larger concentrations it decreases suddenly to a constant value of approximately 4 x 10^{-4} mm m^{-1}.

The CET zone shows an irregular behavior. This is for the mixing of columnar and equiaxed structures that is not constant in the different alloys (the proportion of each structure with respect to another): i.e. at aluminum concentrations equal to and lower than 2 wt%, the wear rates are intermediate to the wear rate of the equiaxed and columnar structures, whereas at 3 wt.% the wear rate is larger and at 4 wt.% lower than that of the equiaxed and columnar structures.

The behavior observed in the equiaxed structure indicates a gradual increase in the strengthening when the amount of alloying increases, whereas when a constant value is achieved, it indicates that the wear mechanism has changed and the wear rate is no longer controlled directly be the alloying. On the other hand, the sudden decrease in the wear rate of the columnar structure when the composition increases from 2wt.%Al to 3wt.%Al indicates a transition in the wear mechanism. The wear resistance is controlled by the strength of the materials, which is formed by the mechanical resistance of the grains and the border of grains. Comparing both structures, an equiaxed structure is preferred in those wear conditions because no sudden transition in wear mechanisms is observed.

All these samples present a discontinuous thin layer of transfer material on the contact surface of the pin composed of iron, zinc and aluminum. This layer is known to influence the wear behavior [70,78]. This kind of layer has been found by other authors [44,45] and this tribolayer has an important role in the wear process although it has been found that in systems that present this layer, the wear rate is controlled mainly by the resistance of the subsurface of the materials [70,79].

3.8. Relationship between corrosion resistance and thermal parameters

Fig. 21(a) shows the correlation between the charge-transfer resistance R_{ct} and the critical temperature gradient. It is observed that in the experiments with Zn–Al hypoeutectic alloys, the R_{ct}

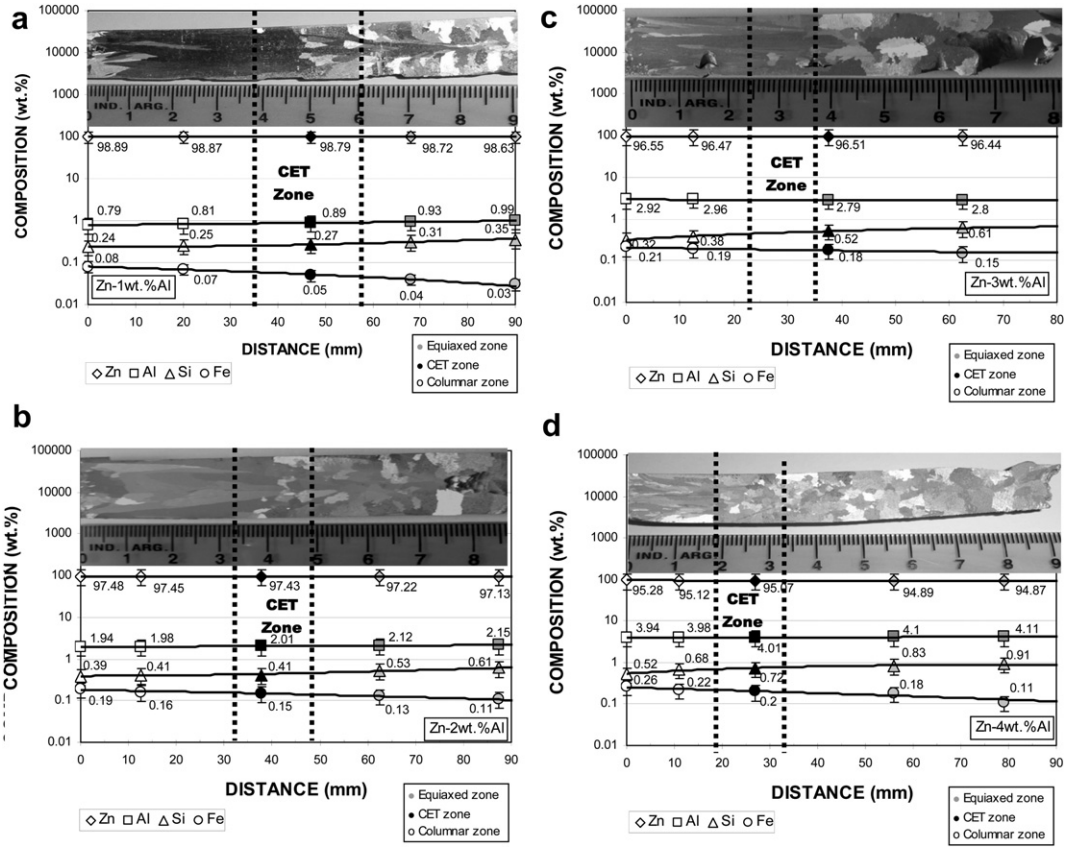

Fig. 19. Composition of the alloy versus distance from the chill. (a) Zn-1wt.%Al, (b) Zn-2wt.%Al, (c) Zn-3wt.%Al and (d) Zn-4wt.%Al alloys.

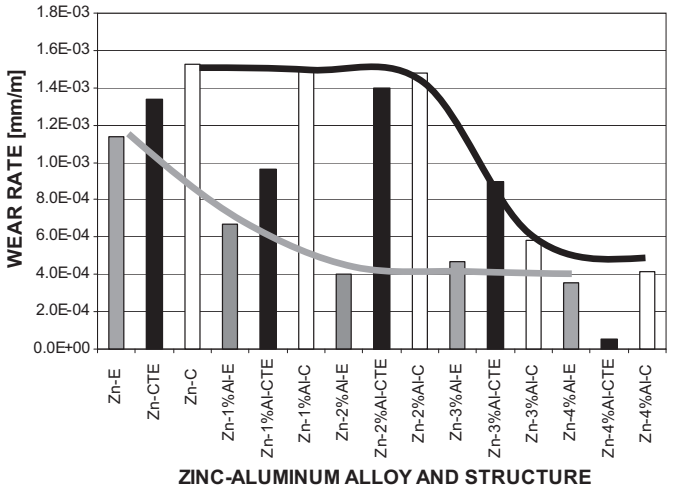

Fig. 20. Wear rate in function of the composition of the alloy (Zn-1wt%Al, Zn-2wt%Al, Zn-3wt%Al and Zn-4wt%Al) and structure (columnar, equiaxed and CET).

increases with the critical temperature gradient from 4wt.%Al to 1wt.%Al alloys. In contrast, the hypoeutectic alloys with the lowest critical temperature gradients are the least resistant to corrosion.

Fig. 21(b) shows that R_{ct} increases with the increase in the average critical cooling rate ($\dot{T}$) from 4wt.%Al to 1wt.%Al alloys. On the other hand, the hypoeutectic alloys with the lower cooling rates are the less resistant to corrosion.

Fig. 21(c) shows the correlation between the variation in R_{ct} and the average liquidus interphase velocity (V_{LC}). It is observed that R_{ct} diminishes with the increase in V_{LC} from 1wt.%Al to 4wt.%Al alloys. In contrast, the hypoeutectic alloys with the highest average interphase velocity are the most resistant to corrosion.

3.9. Relationship between corrosion resistance and structural parameters

Fig. 22(a) shows the variation in the charge-transfer resistance R_{ct} versus the solid fraction (f_S), representing the dendritic region formed. It is observed that R_{ct} increases with f_S from 4wt.%Al to 1wt.%Al alloys. On the other hand, the hypoeutectic alloys with the lowest solid fraction are the least resistant to corrosion.

Fig. 22(b) and (c) shows R_{ct} plotted as a function of grain size (G_S) and secondary dendritic arm spacing (λ_2). It is possible to see that R_{ct} decreases from the columnar to equiaxed zones of the samples, as both G_S and λ_2 increase.

The values of grain size in the CET zones are smaller than in the equiaxed zones and R_{ct} decreases from Zn-1wt%Al to Zn-4wt%Al alloys (black points inside the circle in Fig. 22(b)).

The correlation between R_{ct} and λ_2 shows the same behavior as for G_S (Fig. 22(c)). R_{ct} decreases with the increase in λ_2 and from the columnar to the equiaxed zones of the samples. In this case, the values of the CET zone are between the values of both columnar and equiaxed zones.

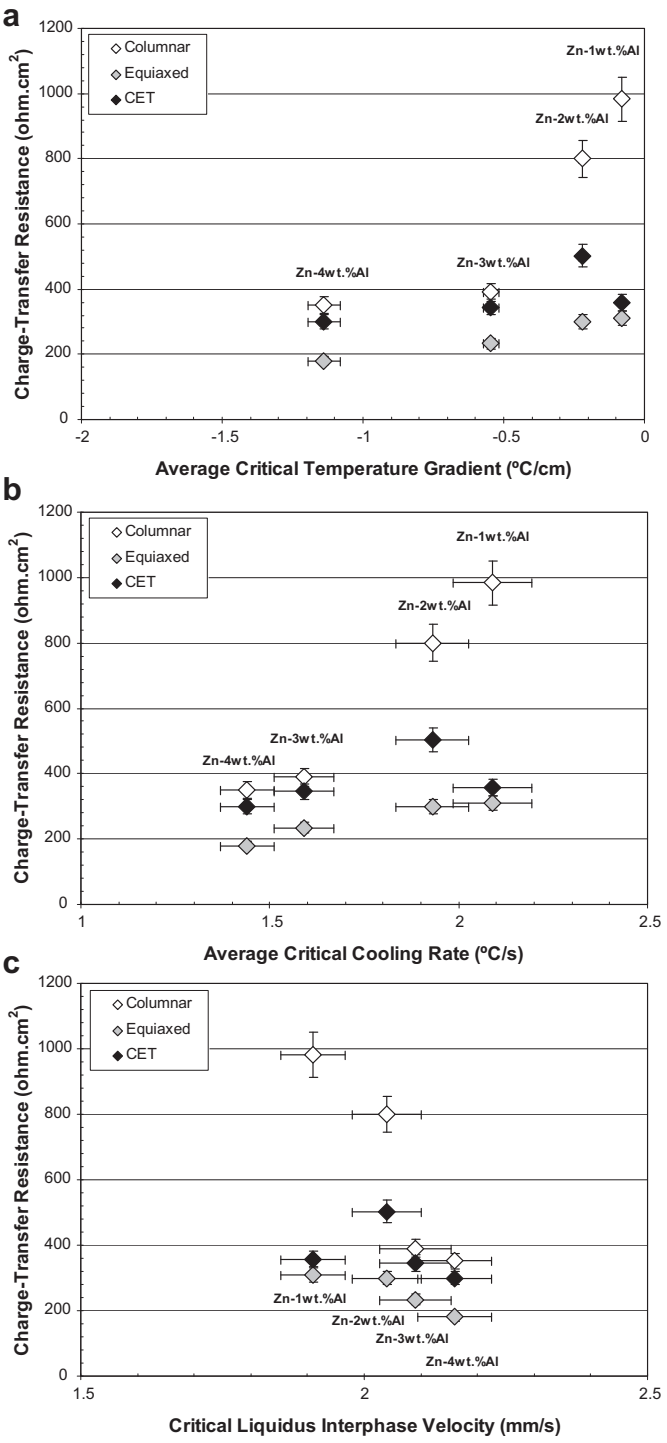

Fig. 21. Correlation between Rct and: (a) Critical temperature gradient (G_c), (b) Cooling rate ($\dot{T}$), (c) Critical liquidus interphase velocity (V_{LC}).

3.10. Relationship between wear rate and structural parameters

Fig. 23(a) shows the wear rate versus the grain size for the three types of structures (columnar, equiaxed and CET). It is observed that the wear rate increases as the G_S increases.

The wear rates of the columnar grains are higher than those of the equiaxed grains for similar grain sizes. It is remarkable that the wear rate of the columnar and equiaxed structures becomes similar at lower grain sizes. In contrast, the wear rate of the CET zone decreases rapidly as the G_S decreases to values lower than those corresponding to the equiaxed or columnar grains. The decrease in the wear rate is attributed to the strengthening by the border grain theory [69], which establishes that the stacking of dislocation in the border of grains causes the strengthening of the material.

Fig. 23(b) shows the wear rate versus average dendritic spacing in each zone of the samples of different alloys. The results show

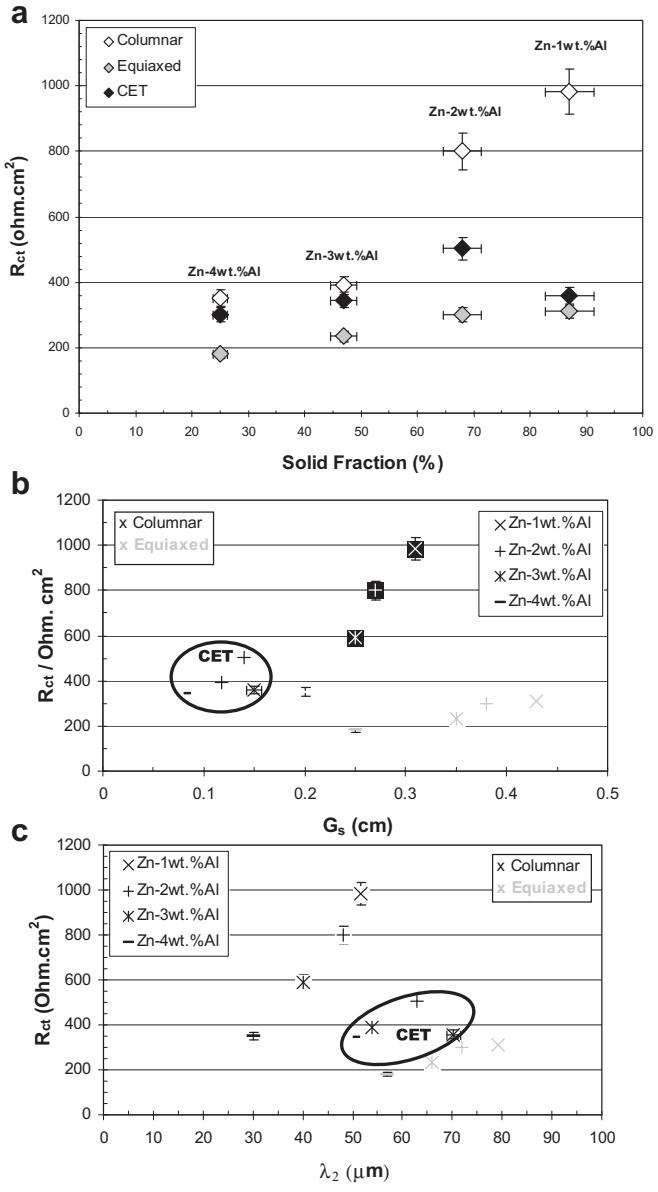

Fig. 22. Charge-transfer resistance (R_{ct}) versus (a) solid fraction (f_S), (b) grain size (G_S) and (c) secondary dendrite arm spacing (λ_2).

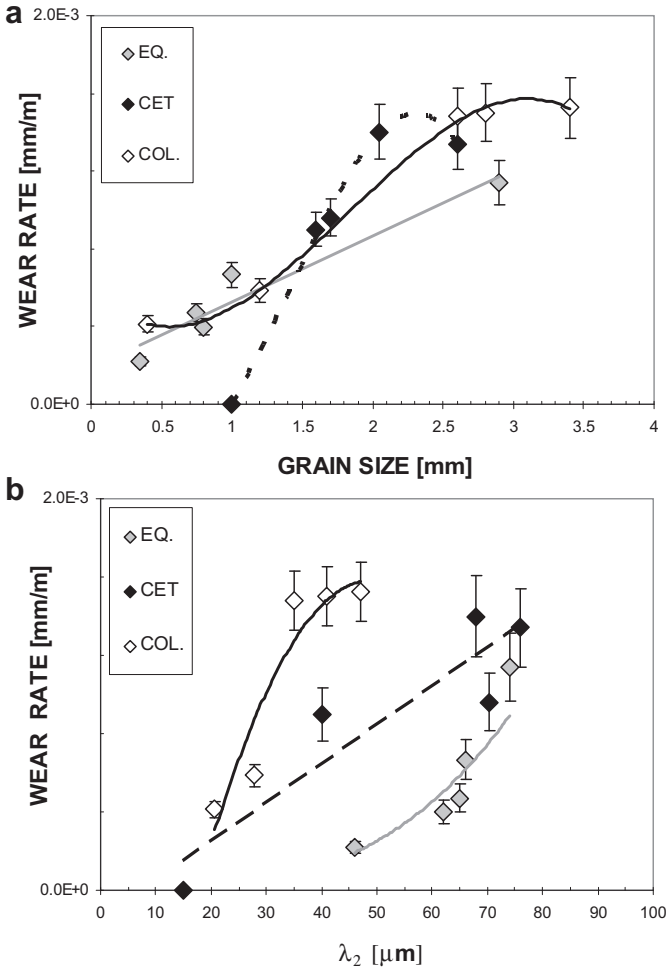

Fig. 23. Wear rate versus (a) grain size and (b) secondary dendritic spacing for three types of structure (columnar, CET and equiaxed) and for all the compositions together.

that the wear rate increases as λ_2 increases, in a stronger relation than in the case of the dependence of wear rate on G_S. In addition, there are clear differences among the types of dendrite (columnar, equiaxed and CET), indicating that for a given spacing, the wear rate decreases in the same order. This stronger relation between λ_2 and the type of dendrite strongly indicates a more fundamental relation between wear resistance and dendritic spacing than between wear resistance and grain size.

The wear rates of the columnar grains are higher than those of the equiaxed grains at a same λ_2, and both converge at similar values when λ_2 decreases. The wear rate of the CET zone is intermediate between the columnar and equiaxed grains.

In diluted Zn–Al alloys it is observed that there is a larger influence of the structure of the subsurface on the wear resistance, in particular when it is related to λ_2 for each structure. The wear resistance of the CET zone has an intermediate value because it is a mix of columnar and equiaxed grains and a non-proportional mix could explain the relation between the wear rate and λ_2.

4. Conclusions

Here we determined the main parameters which characterize the columnar-to-equiaxed transition (CET) phenomenon during the directional solidification process as well as the principal parameters which characterize the corrosion and wear resistance of hypoeutectic Zn–Al alloy samples. We also determined the relation between thermal, corrosion and wear parameters and can draw the following conclusions:

1. Samples of Zn–Al hypoeutectic alloys with CET were obtained and the transition occurs in a zone rather than in a sharp plane, where both columnar and equiaxed grains coexist in the melt. The thermal parameters during the transition vary as follows: the critical temperature gradient in the melt varies between -0.08 K mm^{-1} and -1.13 K mm^{-1}, the critical liquid isotherm velocity varies between 1.91 mm s^{-1} and 2.16 mm s^{-1} and the cooling rate in the melt varies between 1.44 K s^{-1} and 2.09 K s^{-1}, with average transition zones between 27.6 mm and 53.1 mm.
2. The average secondary spacing increases from columnar to equiaxed zones in the samples and the results of the measurements of the grain size show that in the CET region, the equiaxed grains are smaller, and that after the transition, in the equiaxed zone, the grain size either increases or remains approximately constant.

3. From the analysis of the values of charge-transfer resistance, Zn-1wt.%Al alloys with columnar and equiaxed structures are the most resistant to corrosion. In the case of the samples with CET structures, the most resistant to corrosion is Zn-2wt.%Al. However, the charge-resistant transfer criterion for the evaluation of corrosion resistance of the alloys does not indicate the protective characteristics of the films formed on hypoeutectic Zn–Al alloys directionally solidified.
4. From the analysis of the current values in the polarization curves obtained, it is possible to appreciate that, in the case of hypoeutectic Zn–Al alloys, the equiaxed structure is the most susceptible to corrosion. In the alloys analyzed, the values of the currents are similar for the same Al concentration and the most important difference is observed in the distribution of the cathodic current peaks, which indicates the different characteristics of the films formed during the anodic scan.
5. In the case of the correlation between the charge-transfer resistance and the structure, the values of R_{ct} decrease from the columnar to the equiaxed zones of the samples, as both structural parameters (grain size (G_s) and secondary dendrite arm spacing (λ_2)) increase.
6. R_{ct} increases with the increase in G_{LC}, in $\dot{T}$ and in f_S, from 4wt.% Al to 1wt.%Al alloys and decreases with the increase in V_{LC} from 1wt.%Al to 4wt.%Al alloys.
7. For the same wear conditions, the wear rate of the equiaxed region is lower than that of the columnar and transition regions. Independently of the type of structure (columnar, equiaxed or CET), the wear resistance increases with the aluminum concentration. For each alloy concentration, the wear resistance increases from the columnar to the equiaxed structure.
8. A clear inverse relation is observed between the wear resistance and the secondary dendritic spacing, which may explain the increase in wear resistance in the equiaxed region.

Acknowledgments

We would like to thank the National Science Research Council of Argentina (CONICET) for the financial support.

References

[1] J.A. Spittle, Int. Mater. Rev. 51 (2006) 247–269.
[2] S.C. Flood, J.D. Hunt, Columnar to Equiaxed Transition, ASM Handbook, ASM International, Materials Park, OH, 1998.
[3] G. Reinhart, N. Mangelinck-Noël, H. Nguyen-Thi, T. Schenk, J. Gastaldi, B. Billia, P. Pino, J. Härtwig, J. Baruchel, Mater. Sci. Eng. A 413–414 (2005) 384–388.
[4] S. McFadden, D.J. Browne, C.A. Gandin, Metall. Mater. Trans. A 40 (2009) 662–672.
[5] C.A. Siqueira, N. Cheung, A. Garcia, Metall. Mater. Trans. A 33 (2002) 2107–2118.
[6] B. Willers, S. Eckert, U. Michel, I. Haase, G. Zouhar, Mater. Sci. Eng. A 402 (2005) 55–65.
[7] R.B. Mahapatra, F. Weinberg, Metall. Trans. B 18 (1987) 425–432.
[8] I. Ziv, F. Weinberg, Metall. Trans. B 20 (1989) 731–734.
[9] J.D. Hunt, Mater. Sci. Eng. 65 (1984) 75–78.
[10] S.C. Flood, J.D. Hunt, J. Cryst. Growth 82 (1987) 543–551.
[11] S.C. Flood, J.D. Hunt, J. Cryst. Growth 82 (1987) 552–560.
[12] C.Y. Wang, C. Beckermann, Metall. Mater. Trans. A 25 (1994) 1081–1093.
[13] A.E. Ares, C.E. Schvezov, Metall. Mater. Trans. A 31 (2000) 1611–1625.
[14] C.A. Gandin, Acta Mater. 48 (2000) 2483–2501.
[15] A.E. Ares, C.E. Schvezov, Metall. Mater. Trans. A 38 (2007) 1485–1499.
[16] H. Nguyen-Thi, G. Reinhart, N. Mangelinck-Noël, H. Jung, B. Billia, T. Schenk, J. Gastaldi, J. Härtwig, J. Baruchel, Metall. Mater. Trans. A 38 (2007) 1458–1464.
[17] C.A. Siqueira, N. Cheung, A. Garcia, J. Alloys Compounds 351 (2003) 126–134.
[18] J.E. Spinelli, I.L. Ferreira, A. Garcia, J. Alloys Compounds 384 (2004) 217–226.
[19] A. Badillo, C. Beckermann, Acta Mater. 54 (2006) 2015–2026.
[20] M.V. Canté, K.S. Cruz, J.E. Spinelli, N. Cheung, A. Garcia, Mater. Lett. 61 (2007) 2135–2138.
[21] H.B. Dong, X.L. Yang, P.D. Lee, W. Wang, J. Mater. Sci. 39 (2004) 7207–7212.
[22] J. Banaszek, S. McFadden, D.J. Browne, L. Sturz, G. Zimmermann, Metall. Mater. Trans. A 38 (2007) 1476–1484.
[23] M. Wu, A. Ludwig, Metall. Mater. Trans. A 38A (2007) 1465–1475.
[24] V.B. Biscuola, M.A. Martorano, Metall. Mater. Trans. A 39 (2008) 2885–2895.
[25] A. Kumar, P. Dutta, J. Mater. Sci. 44 (2009) 3952–3961.
[26] J.N. Silva, D.J. Moutinho, A.L. Moreira, I.L. Ferreira, O.L. Rocha, J. Alloys Compd. 478 (2009) 358–366.
[27] A. Noeppel, O. Budenkova, G. Zimmermann, L. Sturz, N. Mangelinck-Noël, H. Jung, H. Nguyen-Thi, B. Billia, C.A. Gandin, Y. Fautrelle, Int. J. Cast Met. Res. 22 (2009) 34–38.
[28] H. Jung, N. Mangelinck-Noël, H. Nguyen-Thi, B. Billia, J. Alloys Compd. 484 (2009) 739–746.
[29] S. McFadden, D.J. Browne, Appl. Math. Modell. 33 (2009) 1397–1416.
[30] M. Wu, A. Fjeld, A. Ludwig, Comp. Mater. Sci. 50 (2010) 32–42.
[31] M. Wu, A. Fjeld, A. Ludwig, Comp. Mater. Sci. 50 (2010) 43–58.
[32] A.E. Ares, S.F. Gueijman, C.E. Schvezov, J. Cryst Growth 312 (2010) 2154–2170.
[33] X. Li, Y. Fautrelle, K. Zaidat, A. Gagnoud, Z. Ren, R. Moreau, Y. Zhang, C. Esling, J. Cryst. Growth 312 (2010) 267–272.
[34] H.B. Dong, P.D. Lee, Acta Mater. 53 (2005) 659–668.
[35] S.P. Wu, D.R. Liu, J.J. Guo, Y.Q. Su, H.Z. Fu, J. Alloys Compounds 441 (2007) 267–277.
[36] J.S. Wettlaufer, M.G. Worster, H.E. Huppert, J. Fluid Mech. 344 (1997) 291–316.
[37] X.G. Zhang, Corrosion and Electrochemistry of Zinc, Plenum Press, New York and London, 1996.
[38] M. Sahoo, L.V. Whiting, D.W.G. White, AFS Transactions 93 (1985) 475–480.
[39] B.K. Prasad, A.H. Padwardhan, Y. Yegneswaran, Z. fur Metallkunde 88 (1997) 333–338.
[40] P. Sriram, S. Seshan, H. Md, Trans. Am. Soc. 109 (1992) 769–775.
[41] W.R. Osório, C.M. Freire, A. Garcia, Mater. Sci. Eng. A 402 (2005) 22–32.
[42] W.R. Osório, C.M. Freire, A. Garcia, J. Alloys Compounds 397 (2005) 179–191.
[43] W.R. Osório, M.E.P. Souza, C.M. Freire, A. Garcia, J. New Mat. Electrochem. Systems 11 (2008) 37–42.
[44] M.T. Abou El-khair, A. Danoud, A. Ismail, Mater. Lett. 58 (2004) 1754–1760.
[45] R.A. Auras, C.E. Schvezov, Metallurgical and Materials Transactions A 35 (2004) 1579–1589.
[46] I. Manna, J.N. Jha, K. Pabi, Scripta Metallurgica et Materialia 29 (1993) 817–822.
[47] I. Manna, S.K. Pabi, W. Gust, Int. Mater. Rev. 46 (2001) 53–91.
[48] J. Dutta Majumdar, A. Weisheit, B.L. Mordike, I. Manna, Mater. Sci. Eng. A 266 (1999) 123–134.
[49] J. Dutta Majumdar, R. Galun, B.L. Mordike, I. Manna, Mater. Sci. Eng. A 361 (2003) 119–129.
[50] I. Manna, S.K. Pabi, W. Gust, Acta Metall. Mater. 39 (1991) 1489–1496.
[51] D.B. Williams, E.P. Butler, Inter. Met. Rev. 26 (1981) 153–183.
[52] W. Gust, in Phase Transformations, Series 3, N° 11, vol. 1, The Institute of Metallurgists (ed.), p. II/27, The Chameleon Press, London (1979).
[53] M. Friesel, I. Manna, W. Gust (Colloque), J. de Physique 51 (1990). C1-381-C1-390.
[54] I. Manna, W. Gust, B. Predel, Scripta Metall. Mater. 24 (1990) 1635–1640.
[55] B. Predel, W. Gust, Mater. Sci. Eng. 16 (1974) 239–249.
[56] S.P. Gupta, Acta Metall. 35 (1987) 747–757.
[57] C.P. Ju, R.A. Fournelle, Acta Metall. 33 (1985) 71–81.
[58] I. Manna, J.N. Jha, S.K. Pabi, W. Gust, in: Structure and properties of interfaces in materials, materials research Society Symp. Proc., W.AT. Clark, U. Dahmen & C.L. Briant (eds.), Materials Research Society, Pittburgh, USA 238 (1992) 517.
[59] S.F. Gueijman, C.E. Schvezov, A.E. Ares, Mater. Trans. 51 (2010) 1861–1870.
[60] A.E. Ares, I.P. Gatti, S.F. Gueijman, C.E. Schvezov, Proceedings of the Modeling of Casting, Welding and Advanced Solidification Processes – XII, The Minerals, Metals and Materials Society, Rosewood Drive, Danvers, USA, 2009.
[61] A. E. Ares, L. M. Gassa, S. F. Gueijman, C. E. Schvezov, Proceedings of shape casting: the 3rd International Symposium, The Minerals, Metals and Materials Society, Rosewood Drive, Danvers, MA 01923, USA, 2009.
[62] M.R. Rosenberger, Alicia E. Ares, Isaura P. . Gatti, Carlos E. Schvezov, Wear 268 (2010) 1533–1536.
[63] A.E. Ares, L.M. Gassa, S.F. Gueijman, C.E. Schvezov, J. of Crystal Growth 310 (2008) 1355–1361.
[64] A.E. Ares, L.M. Gassa, Corros. Sci. 59 (2012) 290–306.
[65] R.J. Barnhurst, Zinc and zinc alloy casting, in: R.J. Barnhurst (Ed.), ASM Hand Book, tenth ed., vol. 2, ASM International, The Materials Information Society, Metals Park, OH, 1995.
[66] R.J. Barnhurst, E. Gerevais, AFS Transaction 85-91 (1983) 591–602.
[67] N. Tunca, R.W. Smith, J. Mat Sci. 23 (1988) 111–120.
[68] R. Trivedi, W. Kurz, Int. Mater. Rev. 39 (1994) 49–74.
[69] H.E. Boyer, T.L. Gall, Metals Handbook. Desk Edition, American Society for Metals, USA, 1990.
[70] M.R. Rosenberger, C.E. Schvezov, E. Forlerer, Wear 259 (2005) 590–601.
[71] M. Vandyoussefi, A.L. Greer, Acta Materialia 50 (2002) 1693–1705.
[72] Ch. A. Gandin, ISIJ Int. 40 (2000) 971–979.
[73] W.R. Osório, A. Garcia, Mater. Sci. Eng. A 325 (2002) 103–111.
[74] J. Augustynski, Corros. Sci. 13 (1978) 955–965.
[75] H. Morrow, in: M.B. Bever (Ed.), Encyclopedia of Materials Science and Engineering, vol. 7, MIT Press, Cambridge, Massachusetts, 1986.
[76] I. Epelboin, M. Keddam, H. Takenouti, J. Appl. Electrochem. 2 (1972) 71–79.
[77] L. Fedrizzi, L. Ciaghi, P.L. Bonora, R. Fratesi, G. Roventi, J. Appl. Electrochem. 22 (1992) 247–254.
[78] D.A. Rigney, Wear 245 (2000) 1–9.
[79] B. Venkataraman, G. Sundararajan, Acta Mater. 44 (1996) 461–473.